Heat Transfer Characterization in Jet Flames Impinging on Flat Plates

Akashdeep Singh Virk

Thesis submitted to the faculty of the Virginia Polytechnic Institute and State University in partial fulfillment of the requirements for the degree of

Master of Science

In

Mechanical Engineering

Thomas E. Diller, Co-chair

Brian Y. Lattimer, Co-chair

Scott T. Huxtable

April 28th , 2015

Blacksburg, VA

Keywords: Jet Impingement, High Temperature Heat Flux Sensor, Gas Temperature, Heat Transfer Coefficient, Adiabatic Surface Temperature

Heat Transfer Characterization in Jet Flames Impinging on Flat Plates

Akashdeep Singh Virk

ABSTRACT

The experimental work involves calculation of radial distribution of heat transfer coefficient at the surface of a flat Aluminium plate being impinged by a turbulent flame jet. Heat transfer coefficient distribution at the surface is computed from the measured heat flux and temperature data using a reference method and a slope method. The heat transfer coefficient (***h***) has a nearly bell shaped radial distribution at the plate surface for H/d =3.3. The value of ***h*** drops by 37 % from r/d =0 to r/d= 2. Upon increasing the axial distance to H/d = 5, the stagnation point ***h*** decreased by 15%. Adiabatic surface temperature (AST) distribution at the plate surface was computed from the measured heat flux and temperature. AST values were found to be lower than the measured gas temperature values at the stagnation point. Radial distribution of gas temperature at the surface was estimated by least squares linear curve fitting through the convection dominated region of net heat flux data and was validated by experimental measurements with an aspirated thermocouple. For low axial distances (H/d =3.3), the gas temperature dropped by only 15 % from r/d = 0 to r/d = 2. Total heat flux distribution is separated into radiative and convective components with the use of calculated heat transfer coefficient and estimated gas temperatures. At H/d = 3.3, the radiation was found to be less than 25 % of the net heat flux for $r/d \leq 2$.

DEDICATION

This work is dedicated to my parents and my brother who have always provided me with unconditional love, encouragement and support. It is a blessing to have three of you in my life. I pray God always blesses you.

ACKNOWLEDGEMENTS

I want to thank God, Almighty for everything that He has provided.

Dr Diller, I am very grateful to have worked under a very supportive and motivating advisor like you. Your expertise in the field of Heat Transfer has been very valuable to my work. Your ever readiness to help and open door policy, has helped a lot with the progress of my work. Your suggestions to analyze results in different ways have added immensely to the value of my work and helped grow my analytical skills. I did not know anything about heat transfer measurements before joining your group, and now I am sure I have learnt a lot of skills which will benefit me in the future as well. Working under your guidance, has helped me be a better researcher.

Dr. Lattimer, your suggestions to improve my work have been very helpful. Taking your combustion course has also aided me in my research. Thanks for letting me use the Fire lab to run my tests. I wish to thank Dr. Huxtable for being available at any time to talk about my results.

Thank you to Rachel Wasson, for letting me assist her in performing her experiments, through which I learnt how to make heat flux measurements. Thanks for being there to help me with questions even after graduating, you are a very patient teacher, and I appreciate it. Thanks to Christian Rippe, for letting me use his apparatus to conduct tests, and being there with me at Fire Lab when I ran them. Also, for helping me move stuff to and back from the lab when I did not have a ride. I am sure I caused you a lot of inconvenience sometimes working at late hours, but you were always very helpful. I really appreciate all that you have done to help my work. I also want to thank Rande Cherry and Christopher Cirenza for helping me with calibration of the gauge, and numerous other stuff in the laboratory. You guys are very helpful and I am thankful for having studied with you.

TABLE OF CONTENTS

LIST OF FIGURES

LIST OF TABLES

NOMENCLATURE

AST Adiabatic Surface Temperature

HTHFS High temperature heat flux sensor

c turbulence coefficient

C_p specific heat capacity (kJ/kg-K)

h heat transfer coefficient (kW/m^2-K)

k thermal conductivity (kW/m-K)

m slope

q'' heat flux (kW/m^2)

S elevated temperature sensitivity (μV/(W/cm^2))

S_o room temperature sensitivity (μV/(W/cm^2))

T temperature (^{o}C or K)

t time (s)

L_f Flame Length (m)

H Axial Distance from burner to plate (m)

d Burner nozzle diameter (m)

r radial distance from stagnation point (m)

Greek

δ gage thickness (m)

ε emissivity

ρ density (kg/m^3)

σ Stefan-Boltzman constant (5.67x10^{-11} kW/m^2-K^4)

Subscripts

avg average over the gage thickness

b back (unexposed) surface/jet half-width

diff differential heat flux

exp exposure heat flux

irr irradiation

rad net radiative heat flux

net net surface heat flux

s exposed surface

slug slug heat flux

∞/g gas temperature

rad effective radiation gas temperature

abs-irr absorbed irradiation

Chapter 1– Introduction and Thesis Organization

1.1 Introduction

Heat transfer by flame jet impingement is commonly used in many industrial and domestic heating applications due to its high efficiency. Quantification of the heat transfer characteristics of impinging jet flames can assist in optimization of heat transfer, economy of fuel and control of pollutant emissions. The focus of this research is to experimentally calculate the thermal boundary condition at a flat surface impinged perpendicularly by a turbulent single flame jet. Jet impingement heat transfer on flat surfaces has been studied extensively in the past with instrumentation of various kinds. Multiple gauges make it difficult to make accurate measurements of transient localized heat fluxes. The extreme nature of the fires makes it further difficult to use probes for longer time intervals. Requirements of proper cooling instrumentation make it difficult to make measurements in fires with high heat release rate. High Temperature Heat Flux Sensor (HTHFS) has been used in the past to quantify heat transfer characteristics in diffusion flames impinging on dry wall ceilings. It eliminates the need for multiple gauges and water cooling in temperatures upto 1000^{o} C [2-4]. It has been used to determine heat transfer coefficient and gas temperature distribution on the surface of a flat plate. These quantities lead to separation of convective and radiative components of jet impingement heat transfer. In most of the experimental studies done on impinging jet flames, convective heat transfer has been assumed to provide the majority of heat transfer to the target surface. Quantification of radiation and its contribution to total heat flux could help in increasing the efficiency of jet impingement heat transfer. Estimation of gas temperature theoretically has eliminated the need for measuring gas temperature in thin boundary layers in the wall jet region of the flames. Adiabatic surface temperature serves as a crucial parameter in transferring information between fire and structural FE models. It can be calculated from measured HTHFS data and compared to the gas temperature adjacent to plate.

1.2 Organization

The thesis has been systematically organized and the ideas flow in a logical sequence. Figures are embedded into the text to allow for easy reading. Supplementary material can be found in Appendices. Chapter 2 deals with the characterization of heat transfer in jet flames impinging on

flat plates. Details of experimental and theoretical procedures followed have been given. Results from two different methods of heat transfer coefficient calculation have been presented. AST values were computed and gas temperatures were estimated theoretically to be used for separation of total heat flux into radiative and convective components. Meaningful conclusions and scope for future work are given in Chapter 3.

Chapter 2- Heat Transfer Characterization in Jet Flames Impinging on Flat Plates

2.1 ABSTRACT

The experimental work involves calculation of radial distribution of heat transfer coefficient at the surface of a flat Aluminium plate being impinged by a turbulent flame jet. A high temperature heat flux sensor (HTHFS) uses a hybrid heat flux method (HHF) to measure the transient total heat flux and temperature distribution at the plate surface. Heat transfer coefficient distribution at the surface is computed from the measured heat flux and temperature data using a reference method and a slope method. The heat transfer coefficient (***h***) has a nearly bell shaped radial distribution at the plate surface for a non-dimensional axial distance (H/d) =3.3. At H/d = 3.3, the stagnation point heat transfer coefficient was measured to be $0.094 \pm 0.023\ kW/(m^2K)$ by the reference method and $0.089 \pm 0.006\ kW/(m^2K)$ by the slope method. The value of ***h*** drops by 37 % from r/d =0 to r/d= 2. Upon increasing the axial distance to H/d = 5, the stagnation point ***h*** decreased by 15% to a value of $0.08 \pm 0.019\ kW/(m^2K)$ by the reference method and $0.08 \pm 0.0032\ kW/(m^2K)$ by slope method. Adiabatic surface temperature (AST) distribution at the plate surface was computed from the measured heat flux and temperature. AST values were found to be lower than the measured gas temperature values at the stagnation point. It was concluded that AST values should not be used to separate the net radiative and convective components of total heat flux in jet flames. Radial distribution of gas temperature at the surface was estimated by least squares linear curve fitting through the convection dominated region of net heat flux data and was validated by experimental measurements with an aspirated thermocouple. For low axial distances (H/d =3.3), the gas temperature dropped by only 15 % from r/d = 0 to r/d = 2. Total heat flux distribution is separated into radiative and convective components with the use of calculated heat transfer coefficient and estimated gas temperatures. At H/d = 3.3, the radiation was found to be less than 25 % of the net heat flux for $r/d \leq 2$. Comparisons to past empirical correlations and experimental work were found to be good.

2.2 Introduction

Heat transfer by flame jet impingement is commonly used in many industrial and domestic heating applications such as glass processing, melting metals, domestic geysers etc. Quantification of the heat transfer characteristics of impinging jet flames can assist in optimization of heat transfer, economy of fuel and control of pollutant emissions. Reviews by Chandrashekar [16], Viskanta [15], Baukal & Gebhart [26] and Baukal & Gebhart [27] provide ample information on past semi-analytical, empirical, numerical and experimental studies on jet flame impingement heat transfer. Theoretical and analytical studies of jet impingement heat transfer have been few with most of them neglecting radiation and other modes of heat transfer (including chemical heat release at or near the wall) for simplicity [13].

The focus of this research is to experimentally calculate the thermal boundary condition at a flat surface impinged perpendicularly by a low velocity turbulent single flame jet. A high temperature heat flux sensor (HTHFS) [1] was mounted at the center of the plate and used to measure the transient heat flux and temperatures at the plate surface. The heat flux sensor follows a hybrid heat flux (HHF) method of heat flux measurement [6] and can operate in temperatures up to 1000^{o}C without water cooling [1]. It has been used to experimentally separate the heat transfer components through the calculation of the coefficient of convective heat transfer [2-4]. The two primary mechanisms of heat transfer from impinging flame jets to solid surface are forced convection and radiation. In most of the experimental studies done on impinging jet flames, convective heat transfer has been assumed to provide the majority of heat transfer to target surface.

The equation for net heat flux to a flat surface can be developed considering convection, irradiation and re-radiation from heated surface to be the three primary modes of heat transfer from flame jet to surface. The net heat flux is expressed as a sum of these three components,

$$q''_{net} = h(T_\infty - T_s) + \varepsilon_s q''_{irr} - \varepsilon_s \sigma T_s^{\,4} \qquad (1)$$

In Equation (1), q''_{net} denotes the net heat flux to the surface, q''_{irr} represents the irradiation and ε_s represents the emissivity of the surface. The surface and the flames are regarded as gray and diffuse bodies for simplicity; hence absorptivity of the surface equals emissivity. h represents the heat transfer coefficient between impinging combustion products and the flat surface, $T_\infty$and T_s

are the surrounding gaseous environment and surface temperatures. This is the total heat flux absorbed by the surface, a part of which results in transient temperature rise of the body, while the rest is conducted or convected by the body to surroundings. Most studies neglect re-radiation heat flux, because most of the times the target surface is cooled with water to keep it at low temperatures, and sometimes the heat release rate (HRR) of fires are not high enough to raise the surface temperature substantially. In such studies, the total heat flux to surface has been expressed as a combination of convection and radiation heat flux, combined under a term "exposed heat flux" $\left(q_{exp}^{"}\right)$ given as,

$$q_{exp}^{"} = h(T_{\infty} - T_s) + \varepsilon_s q_{irr}^{"} \qquad (2)$$

Jet impingement heat transfer on flat surfaces has been studied extensively in the past with instrumentation of various kinds. Kilham and Purvis [22] used a transient heat transfer measurement technique without probe cooling to measure heat fluxes inside a fire. Their method could be used to measure heat fluxes over a very short period of time when the flame temperatures were high. Fairweather et al. [23] also used a transient mechanism to measure heat flux from the time rate of change of temperature of the exposed side of a probe. The probe was inserted into the fire for a moment with the use of actuated solenoid valves. Wu et al. [24] measured the heat flux with a water cooled heat flux meter mounted on a copper plate with backside cooled by running water. Due to extreme nature of fires with HRR over 20kW, it is difficult to measure the localized transient heat flux over longer periods of time. Risks of damaging the probes without proper cooling are high. HTHFS overcomes these difficulties with extreme temperatures enduring structural elements. Its compact size helps in giving a good measurement of localized heat flux.

Donaldson et al. [17] developed a correlation for laminar jets based on the local velocity gradients at the wall. He incorporated the effects of turbulence in free jet with a constant 'c',

$$Nu_d = \frac{5.4c\sqrt{Re_d}}{H/d}\left(\frac{Pr_{fluid}}{Pr_{air}}\right)^{1/3} \quad \text{for } H/d > 6.5 \qquad (3)$$

$$Nu_d = \frac{5.4c\sqrt{Re_d}}{6.5}\left(\frac{Pr_{fluid}}{Pr_{air}}\right)^{1/3} \quad \text{for } H/d \leq 6.5 \qquad (4)$$

In Equations (3) and (4), Re_ddenotes the Reynold's no. of the flow, H is the plate to nozzle distance, Pr_{fluid} is the Prandtl no. of impinging fluid, Pr_{air} is the Prandtl no. of air at same temperature as impinging fluid. The value of turbulence constant 'c' needs to be determined experimentally. From Equations (3) & (4), one can conclude that maximum heat transfer occurs at H/d =6.5 (the end of potential core region), since the maximum jet velocity and turbulence are experienced at this axial distance. For distances less than 6.5, the jet turbulence is lesser (reflected by constant 'c' in Equations (3) & (4)) and for distances greater than 6.5, jet centerline velocity drops below maximum (reflected by H/d in Equations (3) & (4)), leading to lesser heat transfer. For a fully developed profile (H/d > 6.5), the Nusselt number ($\boldsymbol{Nu_d}$) as a function of radial distance $\boldsymbol{r}$ from stagnation point is a smooth bell shaped curve. At closer axial distances (H/d < 6.5), the heat transfer at stagnation point is not maximum and secondary peaks appear close to stagnation point on either side. These can be attributed to enhancement of heat transfer by vortices developed at jet half width in incoming jet flow. Secondary peaks become more pronounced as H/d decreases below 6.5.

Decrease in heat transfer (Nu) with radial distance (r) can be attributed to the decrease in velocity gradients at the wall with increases in *r*. For fully developed profiles, the decrease in heat transfer was measured to be 30 % from r/b =0 to r/b =2. (where b denotes the jet half-width) [28, 29, 17].

The fluid dynamics of a single flame jet is very similar to that of an isothermal jet [15]. Experimental measurements of Van der Meer [18] also support this statement although the axial velocity decay in a flame jet is faster than an isothermal jet. The pressure and axial velocity profiles in a single flame jet and isothermal jet are very similar [15]. The primary difference between an impinging isothermal and an impinging flame jet arise from the presence of reaction zone in the flame free jet region and sometimes in the impingement and wall jet regions along with the temperature gradients. Besides convection and radiation, thermochemical heat release (TCHR) might also become an important mechanism of heat transfer in flame jet, if the target surface has a catalytic effect. If an incoming flame jet has highly dissociated components and it impinges on a cold surface which lowers its temperature so that dissociated products can combine exothermically, TCHR will have significant contribution to total heat flux.

The bell shaped heat flux curve for large H/d (>3) was also observed by Hoogendoorn et al. [25]. At a Re = 1860, Hoogendoorn et al. found that for configurations with H/d<3, a minimum was observed in heat transfer at the stagnation point with annular maxima appearing at r/d=0.5. As H was decreased further, the radial distance of maxima from stagnation point increased. Recently Hindsageri et al. [13] demonstrated the application of an inverse heat conduction technique to quantify the heat transfer characteristics of premixed methane-air jet flames impinging on flat quartz plates of varying thickness. Thermal Infrared (IR) camera was used to measure the temperature distribution on the back side of the plate, and the heat flux at the surface was determined by adjusting it to match the theoretical temperature solution to 1D transient conduction equation into an infinite slab with the measured temperature at backside. Experimental measurements of adiabatic surface temperature were used to determine heat transfer coefficient and Nusselt no. distribution on the surface from the heat flux and plate surface temperature. Hindasageri et al. [13] proposed a linear correlation between the non-dimensional radial distance (r/d) and non-dimensional Nusselt no. (Nu/Nu_0) (Here, d denotes the circular burner diameter and Nu_0 is the stagnation point Nusselt no.). The radial distribution of heat flux showed exponential decay with distance from stagnation point which was also found in other experimental studies such as Remie et al [14].

In the wake of World Trade Center (WTC) disaster in 2001, a lot of emphasis has been given to the advancement of structural engineering in designing structures that can withstand fires by modelling the response of structures under realistic thermal loading from fires. Wickstörm et al. [5] had demonstrated that adiabatic surface temperature (AST) is a simple parameter that can effectively represent the mixed convection-radiation boundary condition to which a structural element is exposed during a fire. AST can be considered equal to the temperature that a plate thermometer (PT) placed close to the examined surface will measure provided it has the same convective heat transfer coefficient and emissivity as the surface and experiences the same thermal environment as the surface. AST is crucial in the way it serves as a simple interface between fire and FE structural numerical models. Most fire models compute a multivariable gas temperature which is not convenient to be passed on to 2D FE structural/thermal models which require a single global gas temperature at the boundaries of the structural model. AST has been found to be an easy and efficient mode of transferring intricate information about gas

temperature and heat fluxes from fire model to the structural model. Wickstörm et al. [5] used the AST calculated from PT measurements in a set of experiments involving a square tube section suspended 0.2 m below the ceiling of a fire enclosure with a gas burner operating at HRR of 450 kW, as an input to the 2D FE model of the square tube section, and numerically obtained surface temperatures similar to the PT measured surface temperatures. Thus, the use of AST as an effective boundary temperature to represent the complex radiative-convective environment of an ambient fire has been validated by Wickstörm et al. [5].

In the current experimental study, use of HTHFS as an ideal tool for temperature and heat flux measurements in extreme fires has been validated. Measurement of total heat flux on flat surfaces being impinged by jet flames has been made in the pasts with multiple heat flux gauges. Although water cooled Gardon or Schmidt-Boelter gauges have been used to measure total heat flux alone, they measure heat flux to a cold surface maintained at room temperature. No studies report measurement of transient localized heat fluxes in impinging flame jets. HTHFS usage of a hybrid heat flux method (HHF) to report heat fluxes gives it the ability to report accurate steady or transient heat fluxes independent of the material it is mounted on [6]. The HHF method has been validated by comparing the measured standard heat fluxes with those obtained using a Schmidt-Boelter gauge. Calculation of heat transfer coefficient (h) at the surface from measured net heat flux and exposed gauge surface temperature has been done with the use of two methods developed by Vega et al. [2-4]. The methods have a merit over previous techniques that they require the use of only one heat flux sensor to determine $\boldsymbol{h}$. These methods eliminate the need to measure gas temperature close to surface thereby reducing uncertainties in computed $\boldsymbol{h}$ due to uncertainties in measured gas temperatures. The radial distribution of heat fluxes and heat transfer coefficient was also studied. AST for the current set of experiments were determined using the equations developed by Wickström et al. [11]. The gas temperature distribution along the plate surface was estimated by fitting a least squares linear curve through the convection dominated region of net heat flux versus surface temperature graph. The estimated gas temperatures are used to separate the total heat flux into radiative and convective components.

2.3 Experimental methods

2.3.1 Apparatus

The experimental apparatus shown in Figure 1 is designed to hold the thin Aluminium plate in vertical position when it is impinged by fire. It has been constructed with the use of telescoping Unistrut® tubing which makes it easy to change the height of the burner with respect to ground. The dimensions of the plate are:$0.61\ m \times 0.61\ m$ and the thickness of the plate is 0.0008128 m. To prevent heat conduction losses to the frame, the plate is thermally isolated by placing it on top of a wooden block and is prevented from moving horizontally upon jet impact by securing it in grooves carved in wooden blocks fixed to the frame. Two such wooden blocks can be seen in Figure 2. The horizontal distance of the burner tip from the plate (H) is varied by moving the burner. The diameter of the circular burner (d) is 75 mm.

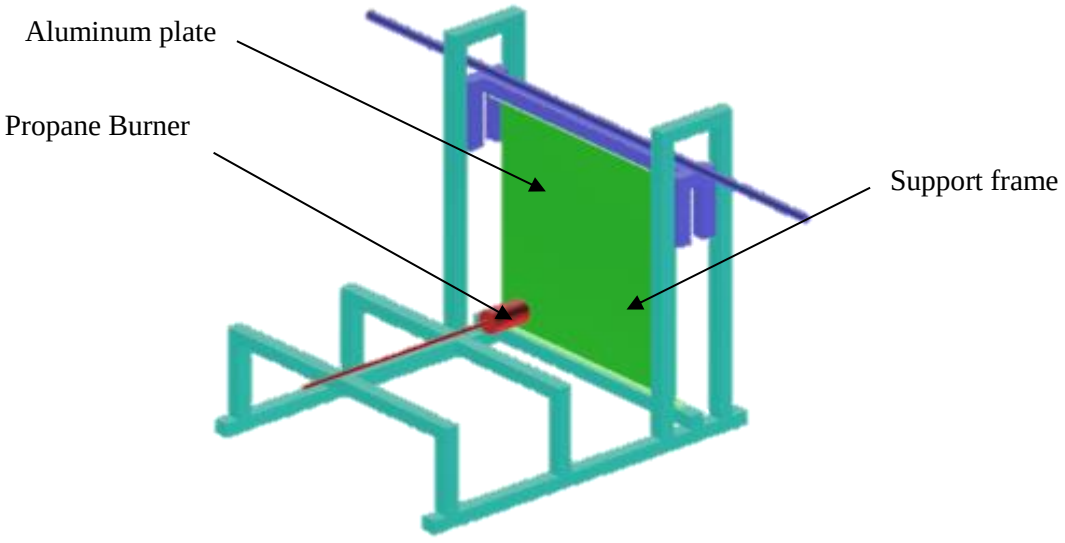

Figure 1. A CAD model of the experimental set-up

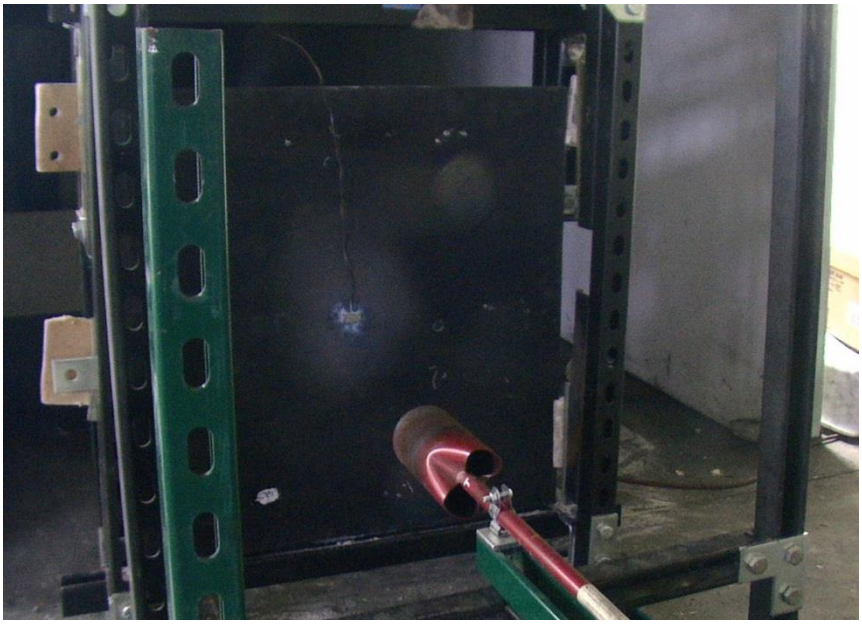

Figure 2. Experimental set-up with the HTHFS mounted at the center of the plate.

The points chosen to study the radial distribution of heat transfer coefficient for an H = 0.254 m were situated on the vertical centerline of the plate at a distance of 0.0508 m (2 inches) from each other (shown in Figure 3). The points have been labelled from 1 to 7, and these numbers will be used to refer to these points in upcoming sections.

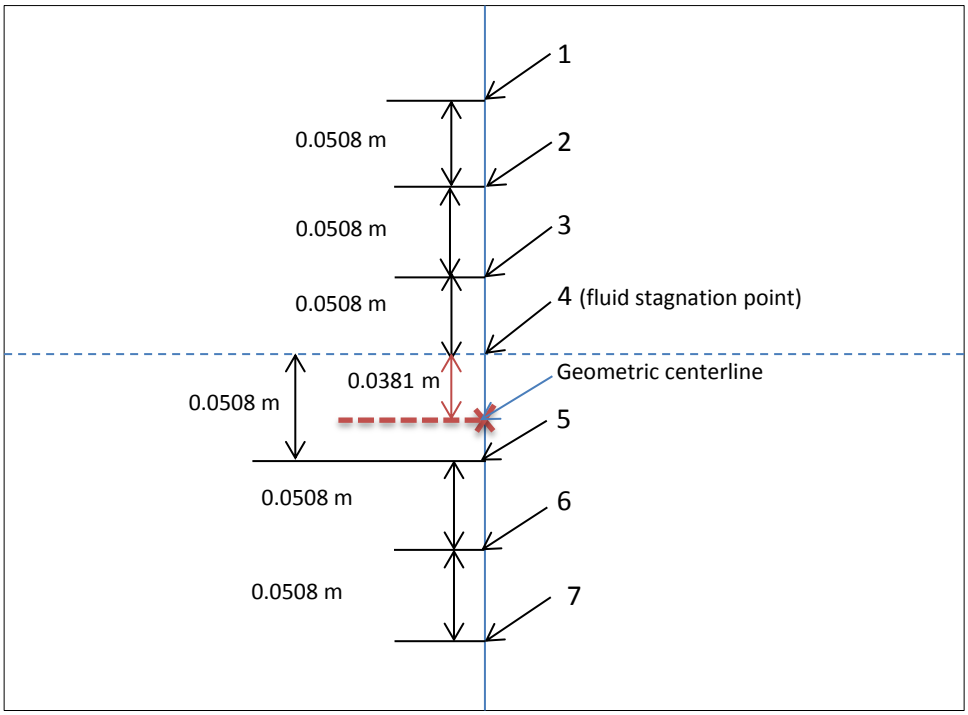

Figure 3. The position of points on the plate at which the heat transfer coefficient is calculated

The flame jet showed a buoyancy of approximately 0.0381 m (1.5 inches) during all the experiments. The burner centerline was moved down by the same distance so that the geometric centerline (the point on the plate coinciding with the burner centerline) lies 0.0381 m below the fluid stagnation point. The fluid stagnation point coincides with the plate center. Propane gas supplied to the burner was set using an Alicat MC-100 mass flow controller with an accuracy of ±0.22% full scale. The burner has a circular outlet and two holes at the backside to allow sucking of air for mixing with the propane jet flowing through a small steel tube connected to the center of the burner. A rear view of the burner is shown in Figure 4.

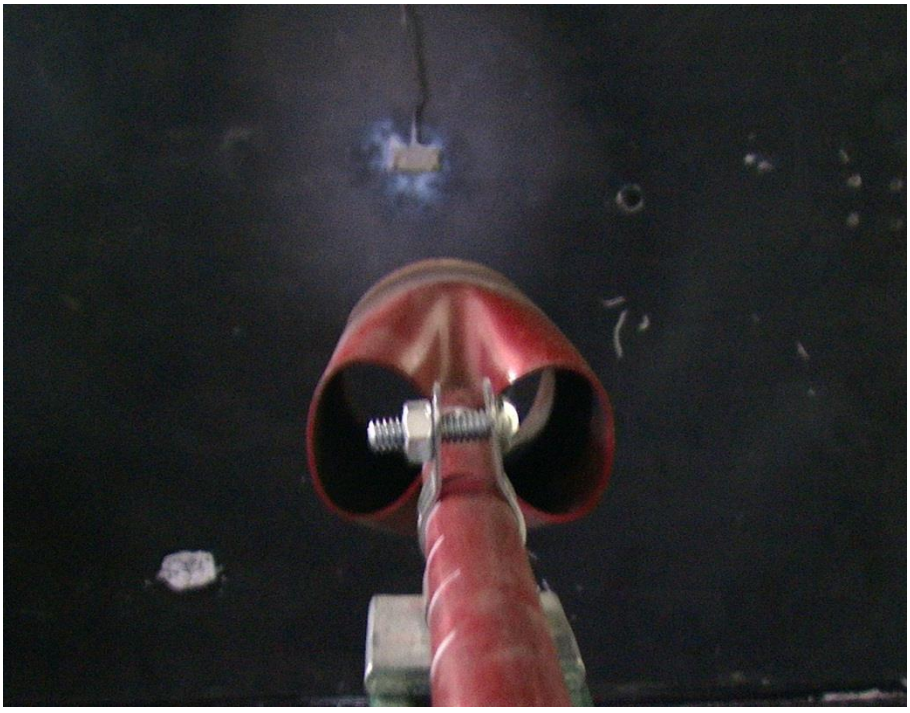

Figure 4. Circular propane jet burner (back view)

2.3.2 High Temperature Heat Flux Sensor (HTHFS)

Non-cooled surface measurements of total heat flux were made at the respective points with the use of a high temperature heat flux sensor (HTHFS) [1, 6]. HTHFS is a total heat flux sensor having a thermopile composed of type K thermocouple elements which is capable of measuring heat flux and temperatures in extreme environments (with temperatures ranging over 1000 ^{o}C) without requiring water cooling [1]. HTHFS design is shown in Figure 5. This sensor uses a hybrid method (a method combining the spatial and temporal temperature measurements of the sensor) to measure heat flux through the surface [6]. The sensor combines the measurement

techniques of two standard modes of heat flux measurement: a differential heat flux sensor and a slug calorimeter.

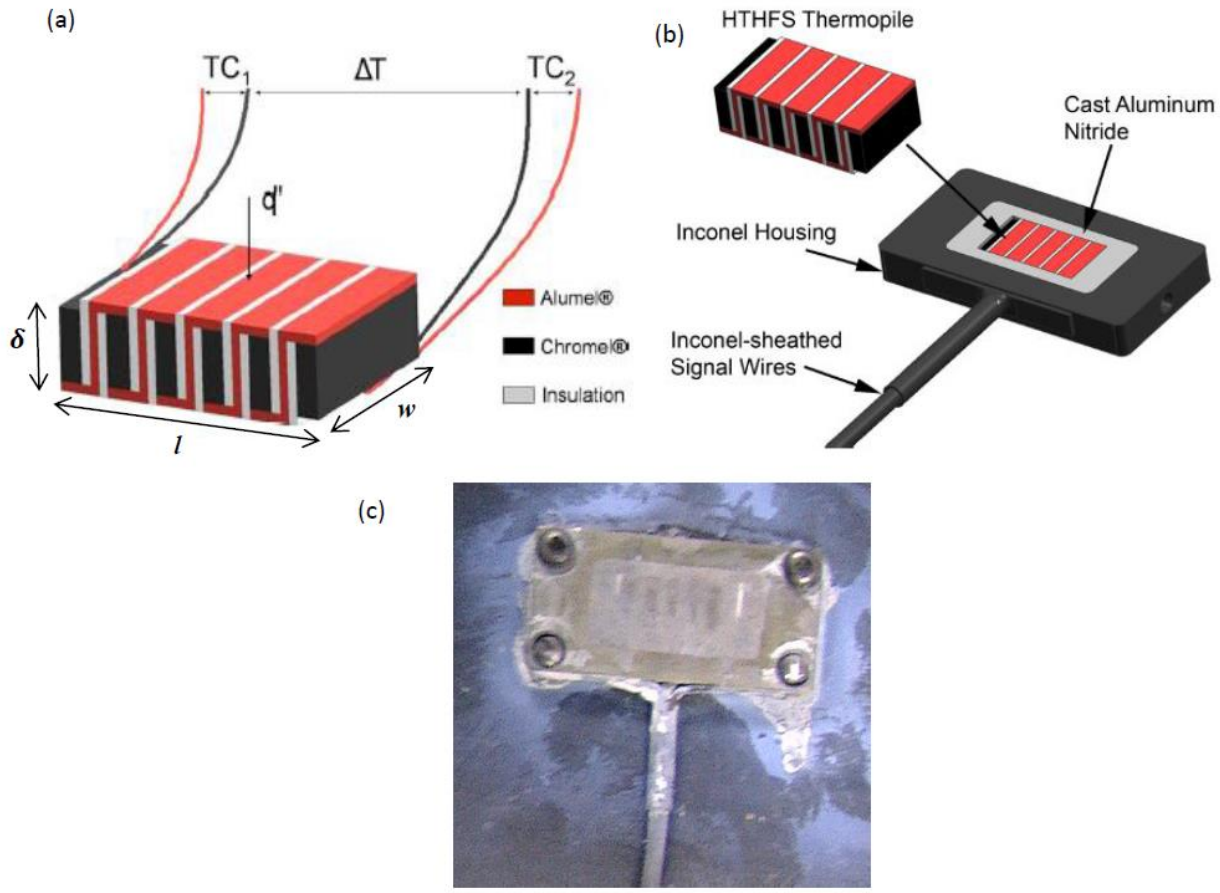

Figure 5.HTHFS design [6] (a) HTHFS thermopile with the attached thermocouples; $\boldsymbol{TC_1 = T_s; TC_2 = T_b}$; **Dimensions of the thermopile are** $\mathbf{l = 9.65\ mm, w = 5.08\ mm,}$ **and** $\boldsymbol{\delta = 3.18\ mm}$; (**b**) HTHFS thermopile in the Inconel housing; Housing dimensions are l=25.4 mm, w= 12.7 mm, and h =3.18 mm. (c) HTHFS mounted with four screws on an Aluminium plate.

A differential heat flux sensor measures the temperatures of the top surface (T_s) and the back surface (T_b), and uses the temperature difference along with the known thermal resistance across the sensor, to calculate the heat flux using the steady state version of 1D Fourier's law of conduction. Differential heat flux can be expressed as,

$$q''_{diff} = \frac{k(T_s - T_b)}{\delta} \qquad (5)$$

where δ is the thickness of the gauge and k is the thermal conductivity of gauge materials.

For HTHFS, the direct voltage output of the sensor ($Voltage$) is directly proportional to the temperature difference developed across the sensor, and the elevated temperature gauge sensitivity (S) gives a measure of the thermal resistance across the sensor, so that the differential heat flux through the sensor can be expressed as,

$$q''_{diff} = \frac{k(T_s - T_b)}{\delta} = \frac{Voltage}{S} \quad (6)$$

The differential aspect of heat flux measurement requires the sensor to be at a steady state, with the heat flux entering and leaving the sensor to be nearly same. This can be accomplished only by mounting the sensor on a good heat sink (a material with a high thermal conductivity). A slug calorimeter measures the amount of thermal energy absorbed by the sensor as a function of time. The rate of change of temperature of the slug multiplied with the thermal mass of the slug per unit area, gives the heat flux into the sensor as,

$$q''_{slug} = \rho C_p \delta \frac{dT_{avg}}{dt} \quad (7)$$

The average temperature of the sensor (T_{avg}) was calculated by taking an average of the top surface temperature (T_s) and the back surface temperature (T_b) of the sensor. The slug aspect of sensor heat flux measurement requires that the sensor's back surface be perfectly insulated so that the heat flux absorbed by the sensor leads to rise of the average temperature of the sensor.

A hybrid heat flux method (HHF) [6] combining both these fluxes (differential and slug) gives the net heat flux as,

$$q''_{net} = q''_{diff} + \frac{1}{2} q''_{slug} \quad (8)$$

Using a hybrid methodology, decreases the dependence of the measured heat flux on the surface on which the sensor is mounted, making it reliable to use under varying experimental conditions. The limiting cases of the mounting surface being an excellent heat sink (requirement for a differential sensor) and thermally non-conducting surface (requirement for slug calorimeter) also gave excellent results with the HHF method. Thus, the HTHFS can be used to make accurate measurements of heat flux under steady-state or transient thermal conditions.

To compute the differential and slug components of the net heat flux $\left(q''_{net}\right)$, the values of elevated gauge sensitivity (S) and the thermal mass of the sensor $\left(\rho C_p \delta\right)$ are required. Both of these sensor properties have been determined through calibration experiments [7]. The sensor was calibrated in a radiative environment in the laboratory to determine its room temperature sensitivity(S_0). This can be used to get the elevated temperature sensitivity (S)using the expression below which was derived in [7]:

$$S = S_0 \left[1 + A\left(T_{avg} - 273\right) + B\left(T_{avg} - 273\right)^2 + C\left(T_{avg} - 273\right)^3 + D\left(T_{avg} - 273\right)^4\right] \quad (9)$$

where the polynomial coefficients are A=3.4923x10^{-4}, B=1.0238x10^{-6}, C= -3.5056x10^{-9}, and D=1.9126x10^{-12}. The sensor's differential sensitivity changes as the temperatures changes because the thermal conductivities of the thermopile elements are a function of temperature. The dimensions of the thermopile were observed to undergo negligible expansion at high temperatures, and thus do not contribute to the change in thermal resistance as temperature of sensor changes. Details of the calibration experiments and room sensitivity values can be found in Appendix C. The emissivity of the gauge surface was determined prior to running the tests. It was found to be 0.77 ± 0.023 through a radiation calibration experiment with the gauge exposed to a halogen lamp. The procedure of emissivity calculations is described in Appendix C.

For validation, heat flux was measured at the same points as the HTHFS using a Schmidt-Boelter thermopile flux gauge (Medtherm model GTW-7-32-485A). The water cooled Schmidt-Boelter gauge was calibrated in a radiative environment prior to use and its room-temperature sensitivity was found to be $1800 \pm 63\ \mu V/(W/cm^2)$. Its surface was known to have an emissivity of 0.94. It has a diameter of 1/2inch and comes attached with two thin steel tubes to maintain a steady flow of water through it. The gauge surface is assumed to stay at room temperature during the experiments, so that the room-temperature sensitivity of the gauge can be used at all times during the experiments. A four screws and metallic block assembly is used to mount the gauge firmly onto any surface.

2.3.3 Gas temperature

It is necessary to measure the gas temperature close to the gauge in order to validate the gas temperature values estimated from HTHFS measured data. The gas temperature was measured 0.0127 m (0.5 inches) away from the surface of the sensor for every test run. Gas temperature

close to the burner outlet was also measured to calculate the density of the combustion products in the flame. The density of combustion products was required to calculate the velocity of jet as it leaves the burner. Measurements of gas temperature were made with aspirated thermocouple probes to minimize radiation errors associated with using bare bead thermocouples [8]. As suggested in Ref. [8], aspirated thermocouples were made using a bare bead Type K thermocouple; with a 0.254 mm diameter Inconel sheathed wires, placed into a 6.35 mm diameter stainless steel tube attached to a pump. The pump drew air over the bead at a velocity of ~15 m/s, creating convection dominated environment thereby reducing radiation heat flux to the bead. The thermocouple bead was located along the centerline of the tube, 19 mm from the tube inlet.

2.3.4 Velocity

The velocity of the flame jet near the burner exit is measured to determine the Reynold's number of the flow. A $19 \times 50\ mm$ bi-directional pressure probe [9] (having an angular insensitivity of about $\pm 50^0$) is used to measure the differential pressure along the jet centerline at a distance of 5 inches from the burner. The bi-directional probe was connected to a Setra Model 264 differential pressure transducer with a range of ± 62.3 Pa, and an accuracy of 0.22 % full scale. Data was collected using a National Instruments 9205 module at a sampling rate of 200 Hz. Velocity was derived from the differential pressure according to the methodology described in [9]. Using the Bernoulli's equation and assuming the pressure effects on density as negligible, velocity (V) should be given as,

$$V = \frac{1}{C}\sqrt{\frac{2\Delta p}{\rho}} \qquad (10)$$

where Δp is the differential pressure, ρ is the density of the combustion products, C is a calibration constant determined in [9] as 1.08. The gas temperature at the same point was measured in a separate test to calculate the elevated temperature density of combustion mixture.

2.3.5 Experimental Procedure

For every experiment, the HTHFS was mounted at the center of the plate. The burner height with respect to the ground was adjusted so that the vertical distance between fluid stagnation point and the gauge center corresponds to the radial distance from fluid stagnation point to the point

under analysis. A two minute baseline for temperatures and voltages of HTHFS were taken before running fire. The desired propane flow rate was then set using the mass flow controller and the fire was ignited to start the jet flame. The flame was allowed to run till the stagnation point temperature on the plate surface reached close to the melting point of Aluminium $(660.3^0\ C)$. This was achieved in about 45 seconds. So each experiment was run for approximately 40 seconds to avoid melting the plate or inducing irreversible thermal deformation. The plate was allowed to cool to room temperature after every experiment. And the gas temperature close to the plate surface was taken in separate tests for each point so as to avoid disturbing the jet flow and resultant heat fluxes. Each experiment was recorded with a RGB camera to notice the flame shape, stability and buoyancy and also assist in locating the stagnation point of the flow.

2.4 Theoretical Methods

2.4.1 Calculation of heat transfer coefficient

The heat transfer coefficient at the plate surface is calculated using two methods developed by Vega et al. [2-4]: a reference method and a slope method. Their application in the current analysis is explained in the following sub-sections.

2.4.1.1 Reference method

After 5 seconds of running the jet flames, the gas temperature close to the plate surface was observed to be fairly steady. Thus after a period of 5 seconds, the gauge experiences steady state gaseous environment, which leads it to experience a constant heat transfer coefficient from the flame. Applying an energy balance at the gauge surface, the net heat flux to the gauge surface is,

$$q''_{net} = \varepsilon_s q''_{irr} - \varepsilon_s \sigma {T_s}^4 + h(T_\infty - T_s) \qquad \left(q''_{irr}\text{, h and } T_\infty \text{ are constant with time}\right) \qquad (1)$$

When the above expression for the net heat flux to gauge is calculated at two or more different points in time during the experiment, a value of heat transfer coefficient (***h***) is obtained.

Thus, at every reference point in time during the exposure, all the other points in time can be used to calculate an ***h*** value,

$$\boldsymbol{h(i)} = \frac{(q_{net}(i) - q_{net}) - \varepsilon\sigma(T_s^4 - T_s^4(i))}{(T_s - T_s(i))} \qquad \text{i=1:N and N=length}(q_{net}) \qquad (11)$$

N is the total no. of data points collected; q_{net} and T_s are the net heat flux and the HTHFS exposed surface temperature at the reference point denoted by ***i***.

For one particular reference point, a graph of ***h*** vs. time at stagnation point is shown in Figure 6,

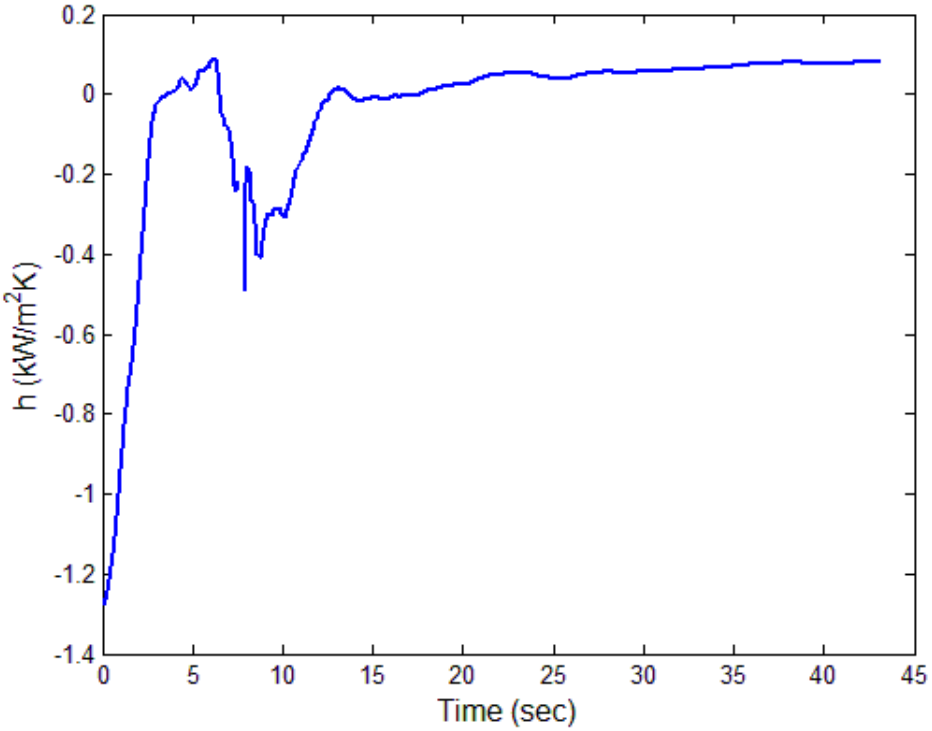

Figure 6. *h* vs. time (calculated by reference method) for one reference point

In Figure 6, the reference point is at time = 7.5 sec. Negative values of ***h*** are computed for points preceding the reference point. For points after the reference point, ***h*** values get steady after a certain period of time (after time = 25 sec). This time period indicates that a certain temperature difference is required between the two points for Equation (11) to give steady values. To get an average value of ***h*** for this reference point, a mean of all the ***h*** values after t= 25 sec is taken. Following the same procedure, an average value of h is calculated at all the points in time. If 'N' no. of data points were collected, we get 'N' no. of ***h*** values one for each point. Neglecting the points that provide a negative average ***h*** value, a typical graph of average ***h*** values vs. time at stagnation point is shown in Figure 7.

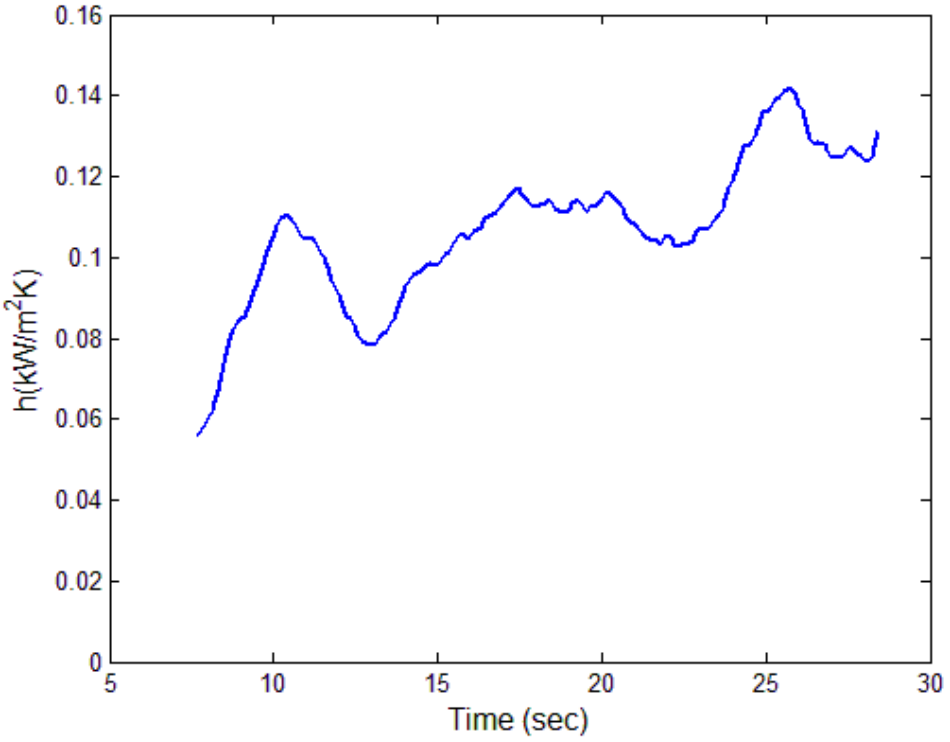

Figure 7. Average *h* value vs. time (reference method)

The respective ***h*** values at all points of time (shown in Figure 7) can then be averaged to obtain the overall heat transfer coefficient during the entire exposure

2.4.1.2 Slope method

The exposure heat flux can be expressed by rearranging the net energy balance in Equation (1),

$$q''_{net} + \varepsilon_s \sigma T_s^4 = \varepsilon_s q''_{irr} + h(T_\infty - T_s) = q''_{exp} \quad (12)$$

Taking the derivative of Equation (11) with respect to the surface temperature(T_s) and assuming the irradiation heat flux and gas temperature as constant,

$$\frac{dq''_{exp}}{dT_s} = -h \qquad q''_{irr} \,\&\, T_\infty are\ constant \quad (13)$$

h can be calculated from the slope of the graph of exposure heat flux (q''_{exp}) vs. surface temperature (T_s). This method assumes constant gas temperature, so it needs to be applied only when the gas temperature has become constant and before the surface temperature of the plate gets steady. Since it takes a few seconds for the gas temperature to reach its steady state value, the initial points of the measured data should not be included in the analysis using this method.

2.4.2 Aspirated Thermocouple time response

The aspirated thermocouple was noticed to be quite slow in recording the instantaneous gas temperature. From the heat flux curves (at the stagnation point), it was noticed that the heat flux reaches its maximum in less than 5 seconds (which is the time the burner requires to provide a stable flame), whereas the gas temperature reported by the aspirated thermocouple required around 38 seconds to reach a steady state value. Since it is a reasonable assumption that the radiation heat flux experienced at the stagnation point is constant during these experiments, the high heat flux to the plate surface can only be explained if the gas temperature is quite high and has reached its steady state value after a few seconds of the start of the experiment. Thus, a few experiments were performed to calculate the time response of the aspirated thermocouple. In these experiments, the burner was allowed to run for 30 seconds, and it was presumed that the gas temperature inside the flame had reached a constant value in this time period. The aspirated thermocouple was then inserted at a point along the centerline of the jet flame and at an axial distance of 0.127 m (5 inches) from the burner tip. The aspirated thermocouple was allowed to stay in the flame till it recorded a steady value. The variation of aspirated thermocouple recorded gas temperature with time is shown in Figure 8,

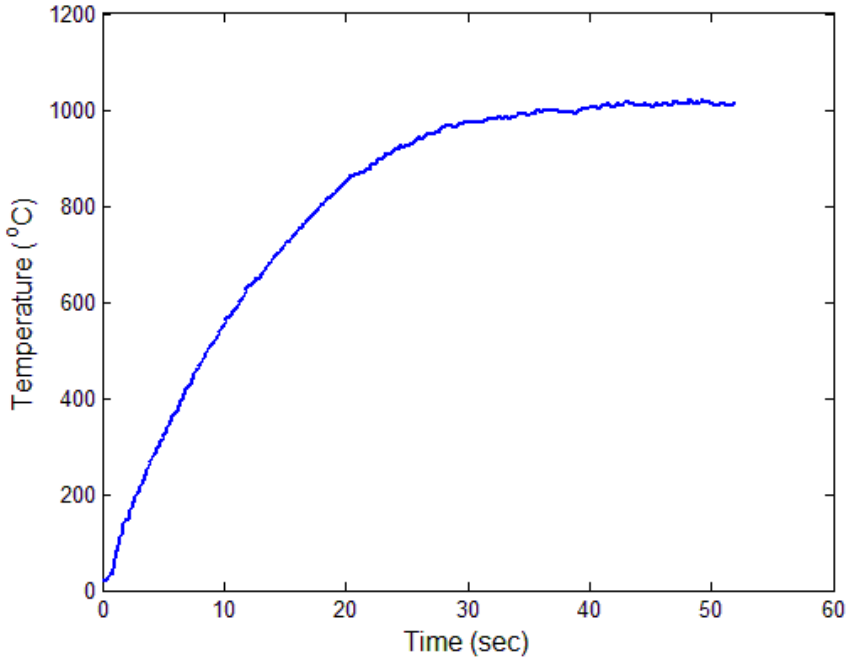

Figure 8. The variation of gas temperature (recorded by aspirated thermocouple) with time

From Figure 8, it can be noticed that it takes the thermocouple nearly 40 seconds to report a steady gas temperature. This test was repeated a couple of times and similar results were observed. The time constant of the aspirated thermocouple can be calculated by assuming that the transient response of the thermocouple (at stagnation point) can be approximated by an exponential curve,

$$T_{gas} = (T_f - T_i)\left(1 - e^{-\frac{t}{\tau}}\right) + T_i \qquad (14)$$

where $T_{gas}$is the gas temperature close to gauge surface ; T_i is the initial gas temperature

T_f is the steady state gas temperature ; τ is the time constant of the aspirated thermocouple.

Equation (14) can be rearranged as,

$$-\frac{t}{\tau} = \log\left(\frac{T_f - T_{gas}}{T_f - T_i}\right) \qquad (15)$$

Taking the steady state temperature from Figure 8 to be 1010 ^{o}C and the initial temperature as 15 ^{o}C, the function $f = \log\left(\frac{T_f - T_{gas}}{T_f - T_i}\right)$ vs. time is plotted in Figure 9.

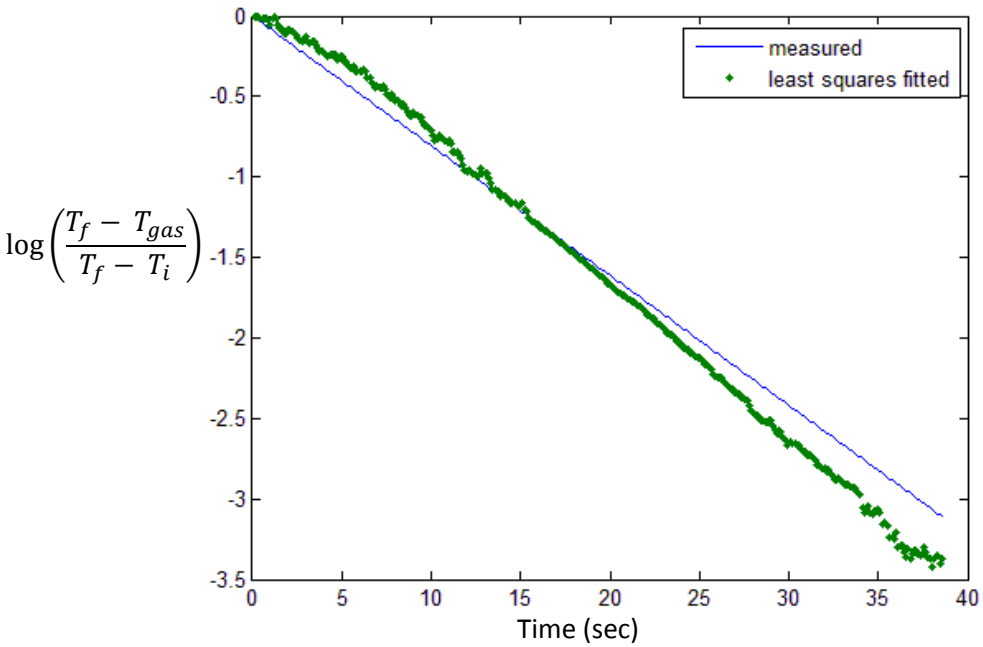

Figure 9. plot of $\log\left(\frac{T_f - T_{gas}}{T_f - T_i}\right)$ vs. time

This is a curve with a continuously increasing slope implying that the time constant is decreasing as time progresses because slope $= -\frac{1}{\tau}$. The slope of the least squares fitted line obtained through the above plot gives the value of the time constant as τ = 12.4 sec. Using this time constant, the corrected gas temperature is plotted using,

$$T = \frac{T_{gas} - T_i}{\left(1 - e^{-\frac{t}{\tau}}\right)} + T_i \qquad (16)$$

Both the temperatures versus time are plotted in Figure 10.

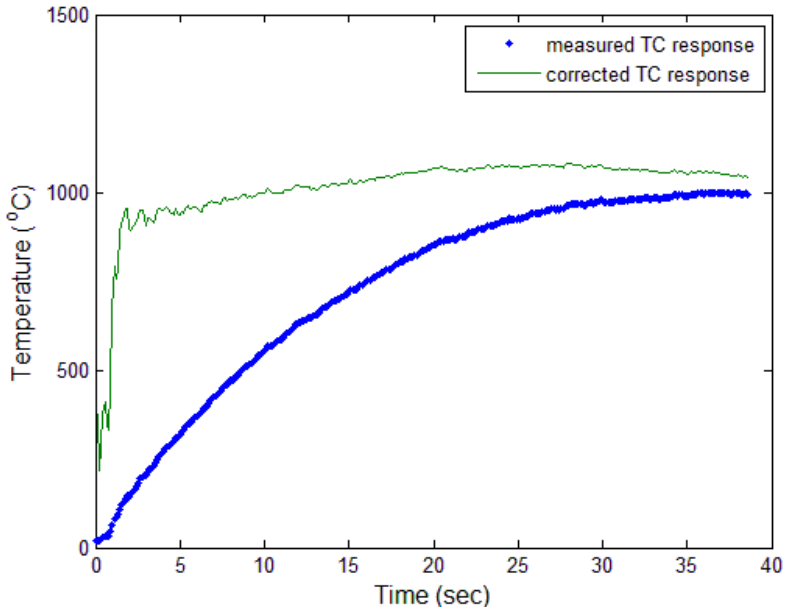

Figure 10. Corrected gas temperature (computed by inverse calculation from recorded thermocouple response) with time

Using τ = 12.4 sec, the actual gas temperature appears to reach the steady state value in a matter of few seconds and stays fairly constant around 1000^o C, although it gives slightly higher values when the thermocouple records steady state temperatures. The higher than expected values at the end can be explained by the error introduced by approximating the thermocouple response curve by an exponential curve with a single time-constant. This value of the time constant of aspirated thermocouple has been used consistently in creating a corrected gas temperature evolution curve from the transient temperature data recorded by the aspirated thermocouple at all the points under consideration. The corrected gas temperature refers to the gas temperature that must have been recorded by the thermocouple had there been no time delay in its response.

2.5 Results

In this section, values of measured heat fluxes and surface temperatures for the HTHFS, the gas temperature close to the gauge surface and the calculated values of heat transfer coefficient (using the two methods described earlier) are presented for all the points under consideration. Adiabatic surface temperatures are also estimated at each point using the method described by Wickstörm et al. [11]. Gas temperature distribution close to the plate is estimated and compared with ASTs. The figures plotted for are from the first out of five repetitions of the experiments.

2.5.1 Heat Fluxes and Temperatures

2.5.1.1 Radial Distribution (Axial distance, H = 0.254 m (10 inches))

An aspirated thermocouple was aligned with the gauge's boundary and placed 0.5 inches from its surface, to measure the gas temperature close to the HTHFS surface. It was believed that placing the aspirated thermocouple close to the stagnation point in the jet flames does not affect the jet flow considerably to alter surface heat fluxes and temperatures. This was also validated by readings of heat fluxes and temperatures taken by HTHFS without the aspirated thermocouple. The gauge surface temperatures and the gas temperature for one particular experiment are shown in Figure 11.

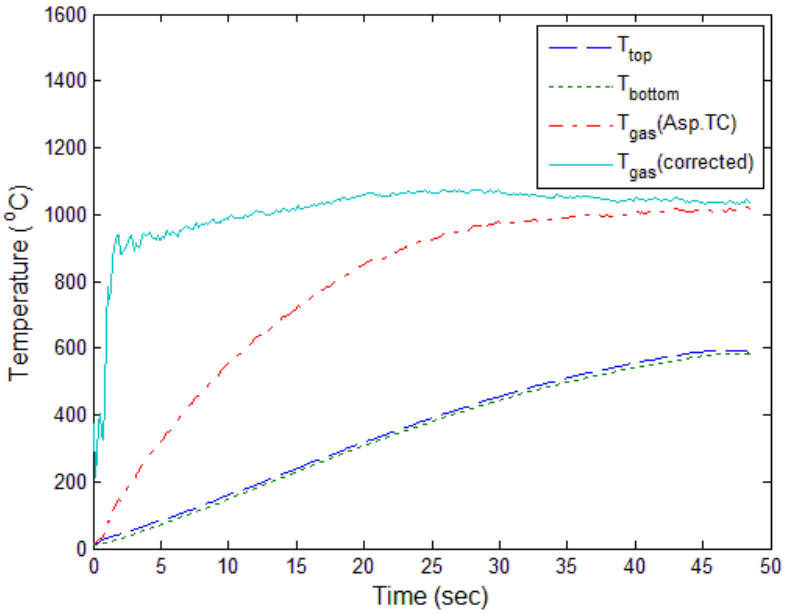

Figure 11. HTHFS surface temperatures and gas temperatures at the stagnation point versus time (H=0.254m)

In Figure 11, T_{top} represents the HTHFS top surface temperature, T_{bottom} represents the HTHFS bottom surface temperature, $T_{gas}(Asp.TC)$ represents the gas temperature close to the HTHFS measured by the aspirated thermocouple, and $T_{gas}(corrected)$ represents the corrected gas temperature calculated by Equation (16) using the time constant $\tau = 12.4$ sec. From Figure 11 above it can be noticed that the gas temperature recorded by aspirated thermocouple takes around 38 seconds to stabilize at approximately 1000^{o}C. The corrected gas temperature has a nearly constant value of 1000 ^{o}C for most part of the experimental run and achieves this steady state value in 2-3 seconds which is the time required for the fire to build up. In Figure 12, the evolution of gauge exposure heat flux calculated using Equation (2) is shown along with the net heat flux to the gauge. The re-radiated heat flux $\left(q^{"}_{re-radiation}\right)$ was calculated using the gauge top surface temperature,

$$q^{"}_{re-radiation} = \varepsilon\sigma T_s^4 \qquad (17)$$

From Figure 12, one can get an insight into the way heat is released when a fire is initiated. Notice that the net heat flux to the gauge rises rapidly to a value of over 120 kW/m^2 in less than 5 seconds. After which it stays nearly constant for some seconds, because the rise in convective heat flux is being balanced by the rise in re-radiated heat flux during this brief period. After 15 sec, the net heat flux falls because the temperature difference between surrounding gas and gauge top surface starts to decline after this time leading to a decline in convective heat flux. The increasing gauge top surface temperature results in increasing re-radiated heat flux which leads to further decline in the net heat flux as time goes on. Flux falls rapidly after 45 sec, because fire has been shut off at this point of time. The re-radiated flux from the HTHFS surface is negligible for the first half of the test, since the gauge surface temperature is quite low initially. But by the end of experiment, it rises to over 20 kW/m^2, since the gauge top surface temperature has elevated to a significant value.

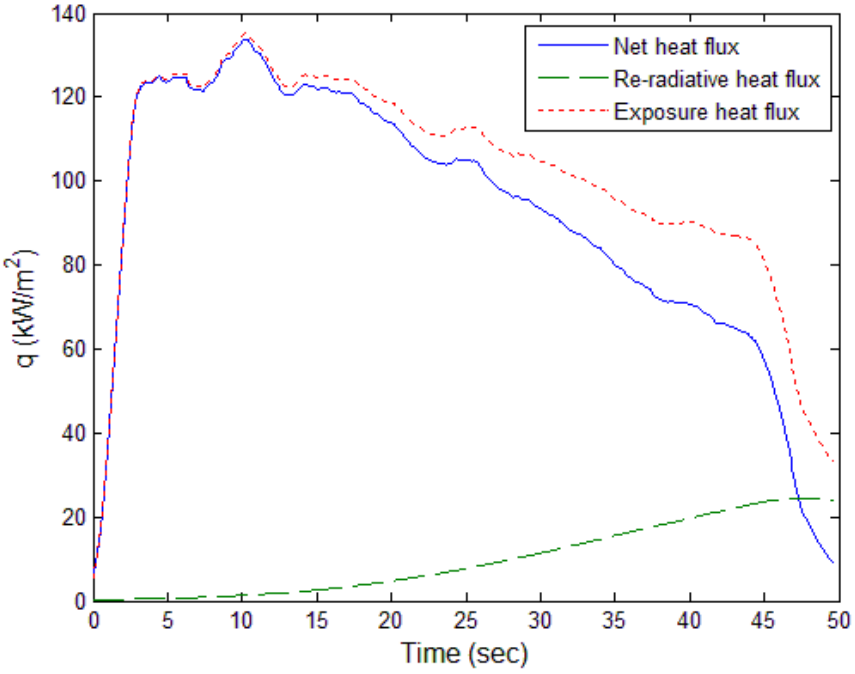

Figure 12 . Exposure heat flux, net heat flux to gauge top surface and heat flux re-radiated by gauge top surface versus time at stagnation point (H=0.254m).

The standard heat flux of the gauge at stagnation point for a constant reference surface temperature, $T_{ref} = 25^0C$ can be calculated from the measured data using the following equations,

$$q''_{net} = h(T_\infty - T_s) + \varepsilon_s q''_{irr} - \varepsilon_s \sigma {T_s}^4 \quad (1)$$

$$q''_{standard} = h(T_\infty - T_{ref}) + \varepsilon_s q''_{irr} - \varepsilon_s \sigma {T_{ref}}^4 \quad (18)$$

Equation (18) - Equation (1),

$$q''_{standard} = q''_{net} + h(T_s - T_{ref}) + \varepsilon_s \sigma({T_s}^4 - T_{ref}^4) \quad (19)$$

The standard heat flux through gauge at stagnation point is shown in Figure 13,

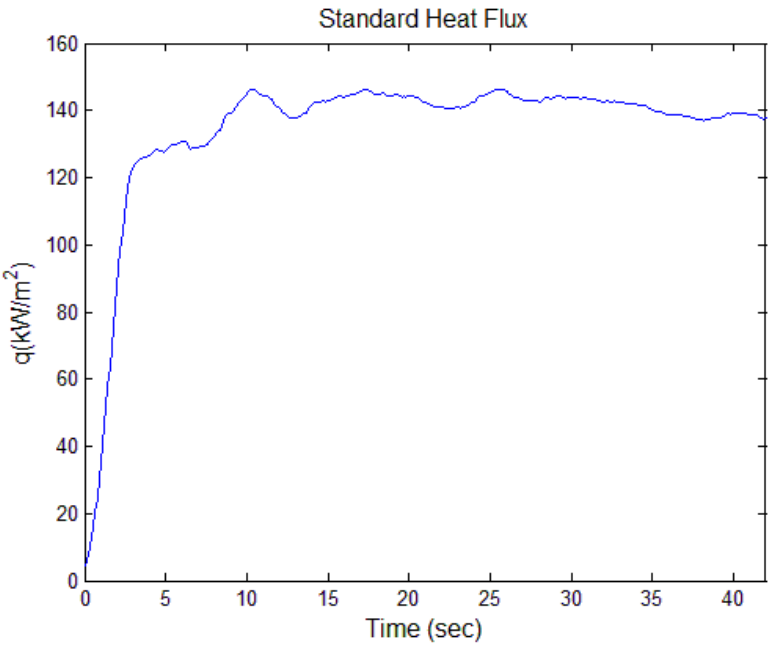

Figure 13. Standard heat flux at stagnation point (H/d = 3.33; H= 0.254 m)

The average standard heat flux is 141 kW/m^2. Measurements of heat flux made with the Schmidt-Boelter gauge showed a steady state total heat flux of 130 kW/m^2, which matches well with the standard heat flux of the gauge. Similar curves for heat flux and gauge surface temperatures were observed at other points with the heat flux maximum, gauge surface temperature maximum and steady state gas temperature decreasing as radial distance from stagnation point increases. The values of the average maxima for the five tests have been shown in Table 1.

Table 1. Average Net heat flux maximum, HTHFS top surface temperature maximum and steady state gas temperature at all points (H=0.254m)

Point #	**Net Heat flux maximum (kW/m^2)**	**Gauge top surface temperature maximum (^{o}C)**	**Steady state gas temperature (^{o}C)**
1	68	320	430
2	90	440	560
3	110	510	720
5	108	490	710
6	89	435	540
7	63	315	420

The measured gas temperatures were observed to be quite less compared to the stagnation point gas temperature even for the points in the stagnation region (i.e. 0.05 m (2 inches) from stagnation point). This could be caused by the aspirated thermocouple measuring the gas temperature outside the thin thermal boundary layer adjacent to plate. The size of the Inconel tube housing the bare bead thermocouple poses restrictions to it being placed inside the thin boundary layer, hence the gas temperature measurements become increasingly erroneous with increasing radial distance.

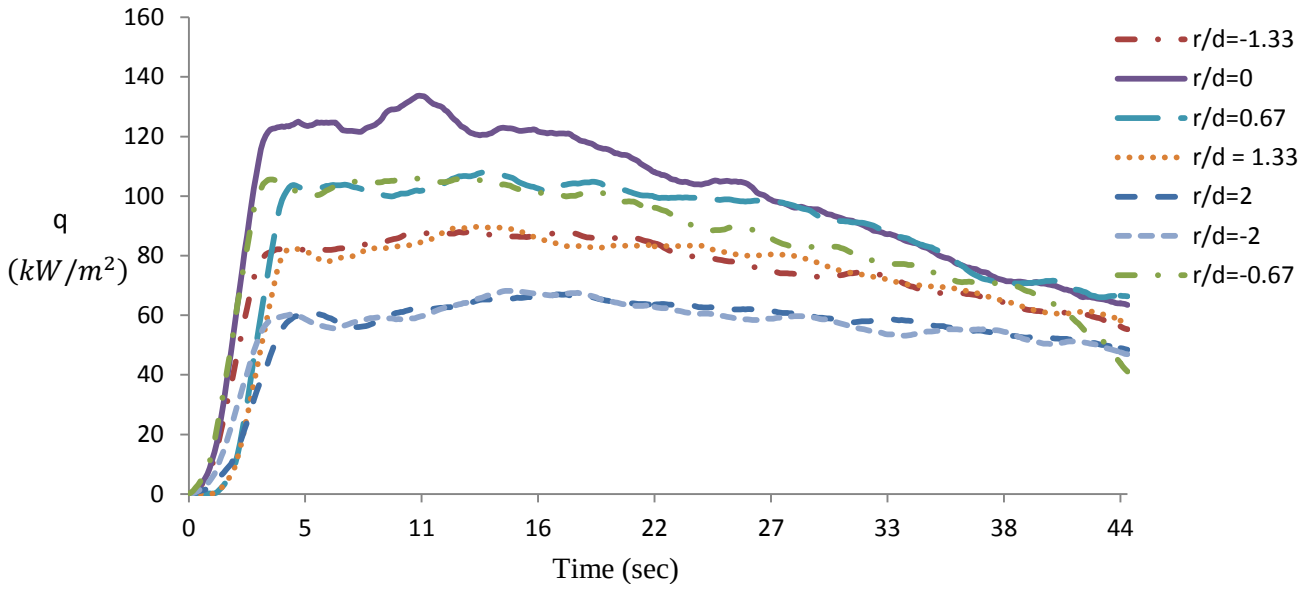

Figure 14 . Total heat flux evolution with time at different radial distances (H=0.254m)

The heat flux data for all the points are plotted together in Figure 14 to get an insight into the heat flux distribution on the plate. Negative values of ***r/d*** represent points that lie above stagnation point. Heat fluxes for points at the same radial distance from stagnation point match well, although the points lying below stagnation point take a little while longer to reach maximum heat flux because of buoyancy effects. The heat fluxes at all points seem to approach towards the same steady-state value.

2.5.1.2 Stagnation point (Axial distance, H = 0.381m (15 inches))

The axial distance of the plate from the burner was increased to 0.381 m so that the plate lies in the established zone of the flame jet. The net heat flux to the plate measured by HTHFS is shown in Figure 15.

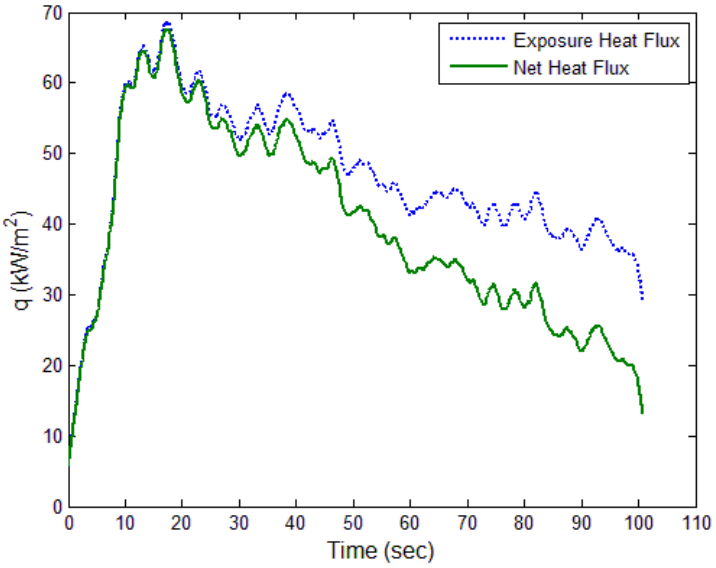

Figure 15. Exposure and net heat fluxes at stagnation point (H = 0.381m)

The axial temperature distribution of the flame jet centerline from burner tip to the plate surface was measured with an aspirated thermocouple and is shown in Table 2,

Table 2. Axial gas temperature distribution for H =0.381 m (15 inches)

Non-dimensional Axial Distance from burner (H/d)	Jet centerline temperature (degree Celsius)
0.67	1120
1.33	1135
2	1160
2.67	1135
3.33	1050
4	1003
4.33	893
4.67	877
4.83	800

The gas temperature was observed to be nearly constant till an axial distance of 0.254 m (10 inches) after which there is a considerable drop because the jet thermal energy diffusion to the

surroundings has reached the jet centerline. The jet centerline temperature after H= 10 inches appears to follow the expression,

$$\frac{T_m - T_\infty}{T_o - T_\infty} = \frac{3.5}{H/d} \qquad (20)$$

In Equation (20), T_m denotes the jet centerline temperature at an axial distance *H*, *d* denotes the nozzle diameter, T_∞ denotes the ambient temperature and T_o denotes jet centerline temperature right outside burner exit.

2.5.2 Heat Transfer Coefficient

2.5.2.1 Axial Distance (H=0.254m (10 inches); H/d =3.33)

Slope method requires a constant gas temperature close to the gauge surface to approximate ***h*** as the slope of the curve of exposure heat flux $\left(q''_{exp}\right)$ versus gauge surface temperature(T_s). Figure 16 shows the graph of $q''_{exp}\ vs.\ T_s$ at stagnation point.

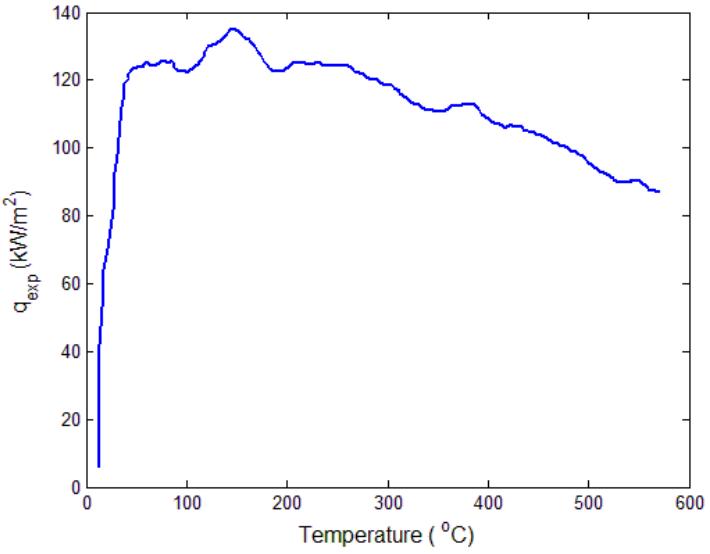

Figure 16. Exposure heat flux versus gauge top surface temperature at stagnation point (H=0.254m)

From Figure 16, it appears that the gas temperature is nearly constant for all times t>5 sec, the gauge top surface temperature when t=5 sec is $T_s = 100^0\ C$. Thus, we can use all the data with gauge top surface temperatures higher than 100^{o}C ($100^0 C \leq T_s \leq 560^0 C$), to calculate a value of heat transfer coefficient using slope method.

For calculating the ***h*** by **reference method**, the previous point considered as reference should experience similar gaseous environment as the current point. And it has also been noticed that the temperature difference between these two points must be larger than a particular value in order to avoid getting infinitely large values of ***h***. We consider the data points recorded after time t=5 seconds for the ***h*** calculation using this method. We also notice that a temperature difference of over 200^o C between the two points is necessary for getting a constant and finite value of ***h*** using this method. Thus, at every point during the exposure, we take all the other points (with temperature difference $\Delta T = 200^o$ C or higher than the respective point) during the exposure as reference and calculate an ***h*** value using the formula,

$$h(i) = \frac{(q_{net}(i) - q_{net}) - \varepsilon\sigma(T_s^4 - T_s^4(i))}{(T_s - T_s(i))} \quad (21)$$

where i=j:N and N=length(q_{net}). Here j = i such that $T_s(i) \geq T_s + \Delta T$

For each point we can average these ***h*** values to get one value of ***h***, and to get an overall ***h*** value for a particular test, we average all the respective average ***h*** values. For the current case, the set of data points that we consider for ***h*** calculation by this method is $100^0 C \leq T_s \leq 560^0\ C$. This region is the same as the region used for the calculation of ***h*** by slope method, and hence a good comparison of values calculated by the two methods can be made. The computed heat transfer coefficients are provided in Table 3, along with the sample standard deviation in five tests at each point and the 95 % level of confidence (k=2) relative uncertainties in the calculation by both the methods (reference and slope).

Table 3. Heat Transfer Coefficients at all points (H=0.254 m)

Point #	Reference Method (kW/m^2K)	Slope Method (kW/m^2K)	Average Standard deviation (%)		Relative Uncertainty (%)	
			Reference Method	Slope Method	Reference Method	Slope Method
1	0.0483	0.0449	7.3	7.7	35	3
2	0.0653	0.0624	7.6	5.8	30	4.1
3	0.0782	0.0773	1.7	3.4	25	5
4	0.0942	0.0892	1.9	4.2	24.2	6.2
5	0.0775	0.0785	4.0	2.5	26	5
6	0.0656	0.0649	3.3	4.1	30.6	4
7	0.0491	0.0513	11.7	11.0	36	3.1

From Table 3, it is noticed that the standard deviation of the five tests was small for both the methods at each point. Thus, the experiments demonstrate good repeatability at each point, which was also evident from the similar heat flux and temperature curves. Uncertainties in reference method ***h*** values are quite high because the sensitivity coefficients of the uncertainty components of ***h*** are inversely proportional to the surface temperature difference between the points in time used for ***h*** calculation. Since the experiments were performed for short intervals of time, a high surface temperature range could not be provided for the reference method ***h*** uncertainties to become lower. Uncertainties in slope method calculated ***h*** are however quite low and within 6 % at all points. At every point, the heat transfer coefficient values determined by the reference method match well with those of slope method. For points lying at equal radial distances from the stagnation point, the heat transfer coefficient values are fairly equal. For points 3 and 5, the ***h*** values drop by 0.82 times their values at stagnation point for Reference method and 0.87 times for Slope method. For points 2 and 6, the values have decreased by a factor of 0.83 for the Slope method and Reference method compared to points 3 and 6. Points 1 and 7 report the lowest values, with Slope method and Reference method values matching well. Compared to points 2 and 6, the values for Slope method and Reference method decrease by a factor of 0.77 and a factor of 0.85. The ***h*** values computed using the two methods are shown in Figure 17 at all the points. Negative values of r/d correspond to points lying above the stagnation point.

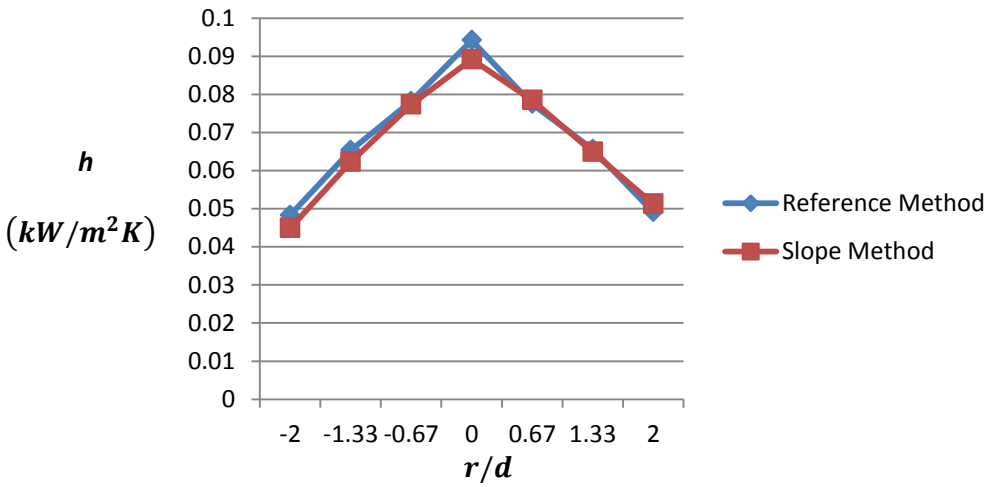

Figure 17. Computed heat transfer coefficient values as a function of non-dimensional radial distance (H=0.254m)

Figure 17, shows the close resemblance between ***h*** distribution for Reference method and Slope method. The ***h*** values for both methods overlap at some points and are very close at others. ***h*** distribution for Reference method and Slope method show a nearly bell shaped curve.

2.5.2.2 Stagnation point (Axial distance, H = 0.381m (15 inches); H/d = 5)

The heat transfer coefficient values found are shown in Table 4. The ***h*** values at stagnation point for H = 0.254m are shown alongside for comparison.

Table 4. Heat transfer coefficient at stagnation point (H = 0.381m)

	H = 0.381 m			H=0.254 m		
	h (kW/m^2K)	Average Standard Deviation (%)	Relative Uncertainty (%)	h (kW/m^2K)	Average Standard Deviation (%)	Relative Uncertainty (%)
Reference Method	0.08	4.1	24	0.0942	1.9	24.2
Slope Method	0.081	3.4	4.1	0.0892	4.2	6.2

The heat transfer coefficient values determined by the methods are close. Standard deviations are low ensuring good repeatability between each test. ***h*** has dropped by 15 % from its value at plate-burner axial distance of 0.254m (10 inches).

2.5.3 Adiabatic Surface Temperature (AST) and Gas Temperature

2.5.3.1 Adiabatic Surface Temperature (AST)

The net heat flux through a solid surface is expressed in Equation (1), rewriting it,

$$q''_{net} = \varepsilon\left(q''_{irr} - \sigma T_s^4\right) + h\left(T_g - T_s\right) \quad (1)$$

Since adiabatic surface temperature is defined as the temperature of a perfectly insulated surface exposed to the same thermal conditions as the surface. Thus, the net heat flux to such a surface will be zero.

$$\varepsilon\left(q''_{irr} - \sigma T_{AST}^4\right) + h\left(T_g - T_{AST}\right) = 0 \quad (22)$$

Subtracting Equation (22) from Equation (1) gives us,

$$q''_{net} = \varepsilon(\sigma T_{AST}^4 - \sigma T_s^4) + h(T_{AST} - T_s) \quad (23)$$

Using the measured surface temperatures(T_s), measured net heat flux(q''_{net}), and the calculated heat transfer coefficient(h), we can solve Equation (23) to get AST at all the points under consideration. For this analysis, the heat transfer coefficient calculated by Slope Method was used. The same set of data points were used in solution of Equation (23), as were used for the calculation of ***h*** in Slope Method. Figure 18 shows the values of AST calculated by solving Equation (23) for an experiment at stagnation point (H=0.254 m).

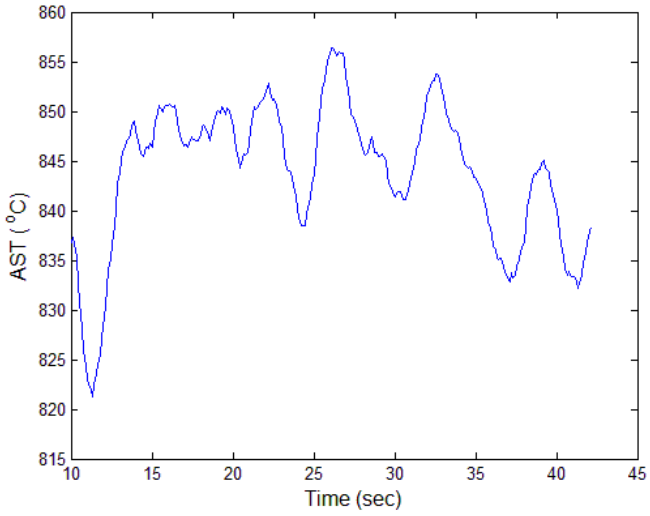

Figure 18. Adiabatic surface temperature versus time at stagnation point (H=0.254m)

Table 5 below show the values of AST calculated from solution of Equation (23) at all points for H =0.254m.

Table 5. AST at all points (H=0.254m)

Point #	**AST (°C)**
1	673
2	759
3	804
4	845
5	807
6	759
7	679

2.5.3.2 Gas Temperature

Gas temperature close to the plate (T_∞) can also be derived from the curve of the measured net heat flux (q''_{net}) versus surface temperature of gauge (T_s). The net heat flux is given as,

$$q''_{net} = h(T_\infty - T_s) + \varepsilon_s q''_{irr} - \varepsilon_s \sigma {T_s}^4 \quad (1)$$

The net radiative component is a sum of irradiation and re-radiation,

$$q''_{net-radiation} = \varepsilon_s q''_{irr} - \varepsilon_s \sigma {T_s}^4 \quad (24)$$

And the convection is given as,

$$q''_{convection} = h(T_\infty - T_s) \quad (25)$$

Assuming the net radiative component of heat flux is small as compared to the convective component, which is true for most experiments of jet impingement heat transfer, particularly for the initial times. The net heat flux is given solely by the convection component,

$$q''_{net} \cong h(T_\infty - T_s) \quad (26)$$

Consequently, the net heat flux curve at initial times is linear and a close approximation of the convective heat transfer component. A least-squares linear curve fitted through a small set of initial data points approximates the convective component and when this is extended to meet the surface temperature axis, it would intersect the axis at a value equal to gas temperature. Such a linear curve is depicted in Figure 19 for an experiment at Point 4 (H=0.254m). The gas temperature obtained from Figure 19 is 1064^o C. This gas temperature was substituted in Equation (1) and a value of the net radiative component $\left[\varepsilon\left(q''_{irr} - \sigma T_s^4\right)\right]$ of the heat flux was calculated for the small set of data points. For the selected group of data points, it was found to be around 25 % of the measured net heat flux. The gas temperature measured at the stagnation point (1070^o C) lies close to this estimated gas temperature. Hence, it can be inferred that least-squares linear curve fitted through a segment of net heat flux versus surface temperature graph over which the radiation contributes less than 25 % of the net heat flux could provide a good estimate of the gas temperature.

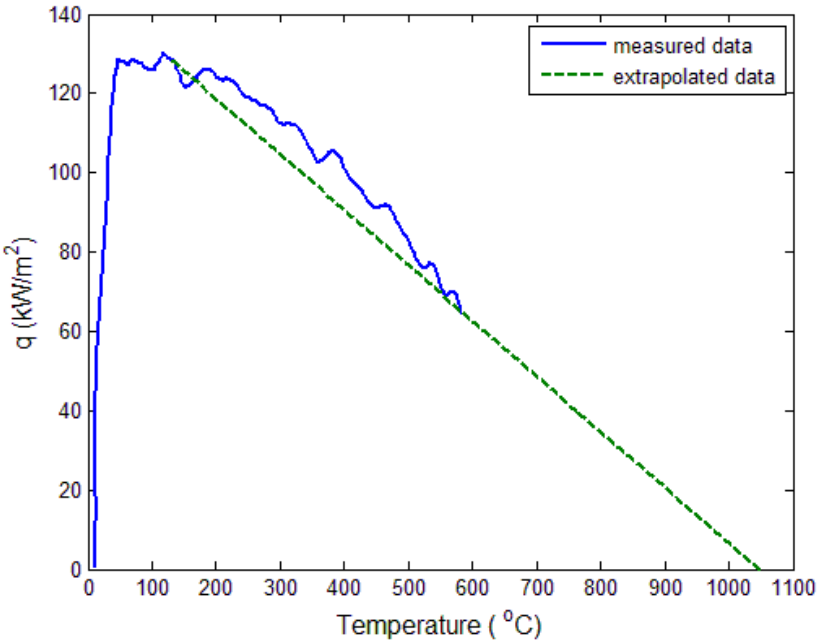

Figure 19. Measured net heat flux data along with linearly extrapolated net heat flux data versus surface temperature.

The slope of the linear fitted curve was found to be higher than the heat transfer coefficient by a value of 30 %. Approximating net heat flux curve as a linear convective heat flux curve leads to over-prediction of measured convective heat flux by 30% which is nothing but compensation for the neglected radiation heat flux (which is 30 % of measured convective heat flux). The radiation heat flux would form a smaller percentage of net heat flux at points away from the stagnation point. Therefore, this method can be applied to other points along the surface where the thin boundary layer of the wall jet makes it difficult to experimentally measure gas temperature. The estimated gas temperature is used to obtain the value of absorbed radiation heat flux. Rearranging Equation (1),

$$\varepsilon_s q''_{irr} + h\,T_\infty = q''_{net} + hT_s + \varepsilon_s \sigma {T_s}^4 \qquad (27)$$

The values of the quantities on the right hand side Equation (27) have been measured experimentally. The estimated gas temperature (T_∞) is then substituted into Equation (27) to obtain a value of the absorbed irradiation (q''_{irr}).The values of gas temperatures estimated at all the points for H=0.254m following this approach, are presented in Table 6, along with the absorbed irradiation values calculated from Equation (27).

Table 6. Estimated gas temperature and absorbed irradiation at all points (H=0.254m)

Point #	**Gas Temperature (degree Celsius)**	**Absorbed irradiation (kW/m^2)**
1	942	16.2
2	996	30.3
3	1028	39.5
4	1062	42.0
5	1038	39.0
6	981	31.0
7	924	17.2

The decrease in absorbed irradiation is insignificant for $r/d \leq 1.33$ (the impingement region) after which the drop is notable. The net heat flux is separated into its components: radiative and convective, by utilizing the values of gas temperature and absorbed irradiation given in Table 6. The convective and radiative components of net heat flux are given in Equations (25) and (24) and are plotted in Figure 20, at the stagnation point (H=0.254m).

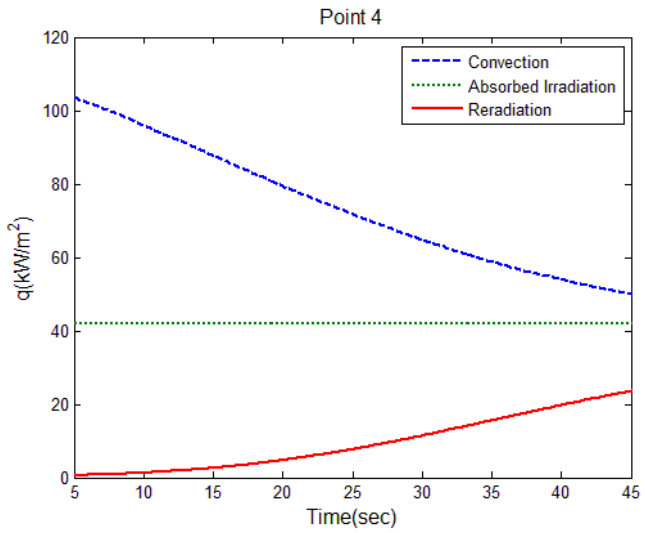

Figure 20. Components of net heat flux at stagnation point (H=0.254m) separated using the gas temperature and absorbed irradiation.

According to the jet flames theory, the jet centerline gas temperature should stay constant at flame temperature for axial distances (H/d) less than 4.5. The gas temperature was measured (with an aspirated thermocouple) along the axis of the flame jet from burner tip to the plate (values shown in Table 7).

Table 7. Gas temperature axial distribution

Axial Distance (H/d)	**Steady state Temp. (degree Celsius)**
0.67	1180
1.33	1154
2	1120
2.67	1076
3.2	1060

The gas temperature stays fairly constant along the flame jet centerline axis with a mean value of 1120^{o} C. A drop of 100^{o} C is observed while moving from burner tip to plate, but this could be attributed to thermocouple measurement errors. AST computed using Wickstörm et al.'s [11] approach (Equation (23)) is much less compared to the measured gas temperature. Use of AST as the effective radiation gas temperature gives an absorbed irradiation of 78 kW/m^2 (compared to 42 kW/m^2 for a gas temperature of 1120^{o}C). It can be inferred that for purposes of determining net radiative component of net heat flux, AST should not be used to separate net heat flux into its radiative and convective components. Shown in Table 8 is the adiabatic surface temperature calculated from Equation (23) and gas temperature estimated by linear extrapolation at stagnation point (Axial distance, H = 0.381m (15 inches)).

Table 8. AST and estimated gas temperature at stagnation point (Axial distance, H = 0.381m (15 inches))

AST (^{o}C)	632
$\boldsymbol{T_{gas}}$**(^{o}C)**	840

AST seems to be quite low compared to the aspirated thermocouple measured gas temperature (800^o C). The linear extrapolation gives a better estimate of gas temperature adjacent to the plate. By least squares fitting of a polynomial curve through the measured heat flux data, a value of $\varepsilon_s q_{irr}^{"} + h\, T_\infty = 87 kW/m^2$ is computed. Gas temperature (measured with aspirated thermocouple) gives an absorbed irradiation equal to 26 kW/m^2. Radiation flux has dropped to half of the value when the burner- plate distance was 0.254m (10 inches) because the flame length of the jet (L_f) was observed to be approximately 0.305 m (12 inches).

2.6 Discussion

Each experiment was recorded with a RGB video camera to facilitate commenting on the effect of flame shape and stability on the heat transfer. Due to low jet velocity, the buoyancy effects of the cold air in the room, was found to have a significant effect on jet. The impingement region's position on the plate gets displaced upwards by 1 and ½ inches and was found to experience some instability in the impingement zone. Rigby and Webb [15], in their study of diffusion flame impingement, had observed that as the nozzle to surface spacing was increased, the flame became more unstable due to buoyancy effects and the impingement region became unsteady. Entrainment of air within the reaction zone of flame leads to decrease in temperatures and over-prediction of heat fluxes in numerical results, which is hopefully avoided in these experiments. The flame jet was found to have a Re=3300 and belongs to the turbulent regime. The slots at the back side of the round burner provide inlets for air to be entrained by the incoming fuel vapor stream. Some turbulence is introduced into the jet by this pre-combustion mixing. In previous literature, turbulence in jets was found to affect flame structure and stability. Van der Meer [18] found out that a jet with higher initial turbulence spreads wider and its axial velocity and temperature decays faster than a jet with low initial turbulence. Thus, such a jet with high initial turbulence would give less heat transfer than one with low initial turbulence. The initial turbulence that the jet in current experiments possesses is believed to be one of the many factors leading to maxima in heat transfer at stagnation point. No soot formation was observed in these experiments, so the issue of soot deposition on the gauge altering its emissivity was not encountered.

Most of the previous experimental work done in impinging jet flames has either neglected radiative heat transfer owing to non-luminosity and low opacity of the gaseous flames. Baukal

and Gebart [19] in their study of non-luminous radiation flux from oxy-enhanced natural gas-air flames found that for higher heat release rate ($HRR = 15 - 25\ kW$), the radiation flux was constant with axial distance. No comprehensive reports quantifying the radiation heat transfer in flame jet impingement have been found in literature which is assumed negligible compared to the convective heat transfer. No comparative study discussing the contribution of radiative and convective heat flux to net localized heat flux is known.

For smaller H/d, cool central cores have been observed in some experimental works, since longer H/d provide for more time for surrounding air to mix and react with the fuel jet. Such a cool central zone leads to annular maxima heat transfer zone; the heat transfer at stagnation point gets lowered due to unburnt cold gases impinging at this point. No such effect on heat transfer distribution was observed in current experiments likely due to some mixing of the air and fuel in the nozzle prior to combustion.

2.6.1 Comparison to past studies

2.6.1.1 Comparison to Rachel et al. [30]

Rachel et al [30] performed experiments to separate heat transfer components in diffusion flames impinging on dry wall ceilings. Fire heat release rates (HRRs) of 50 kW and 90 kW and free flame length to ceiling height ratios, Lf/H, of 2, 1.5, and 1 were investigated to determine the effects they might have on the components of heat transfer at the impingement point. The measured net heat flux and surface temperature data at the dry wall impingement point from one of the experiments of Rachel et al. [30] are used to estimate gas temperature close to the surface. The initial data ($200^0\ C < T_s < 350^0 C$) from the net heat flux versus surface temperature curve from one experiment (50 kW HRR at Lf/2) is extrapolated linearly to intersect the surface temperature axis. This gives an estimate of the gas temperature which is then compared with the gas temperature measured (using an aspirated bare bead thermocouple) at a distance of 0.0127 m (0.5 inches) below the dry wall surface. Figure 21 depicts the curve of net heat flux versus surface temperature (T_s) for one such experiment along with the linearly extrapolated curve meeting the T_s axis at a value of 640^o C. The measured gas temperature was 580^{o}C; this is quite close to the value determined by linear extrapolation. Since Rachel et al. measured the gas temperature at a distance of 0.0127 m from the surface, the actual gas temperature close to surface is suspected to be higher than the measured gas temperature. Convection serves as the

dominant mode of heat transfer to surfaces in jet flames and diffusion flames and hence extrapolating a least-squares line, fitted through a segment of net heat flux curve where radiation is less than 25 % of net heat flux, provides a fairly accurate value of gas temperature. The AST in this experiment was calculated to be 530^o C. This value is a little less than the measured gas temperature. For the measured values of $\varepsilon_s q''_{rad} + h\,T_\infty = 46 kW/m^2$ and h = 0.055 kW/m^2K, the estimated gas temperature gives an absorbed irradiation ($\varepsilon_s q''_{rad}$) equal to 11 kW/m^2 and AST gives a value of 17 kW/m^2.

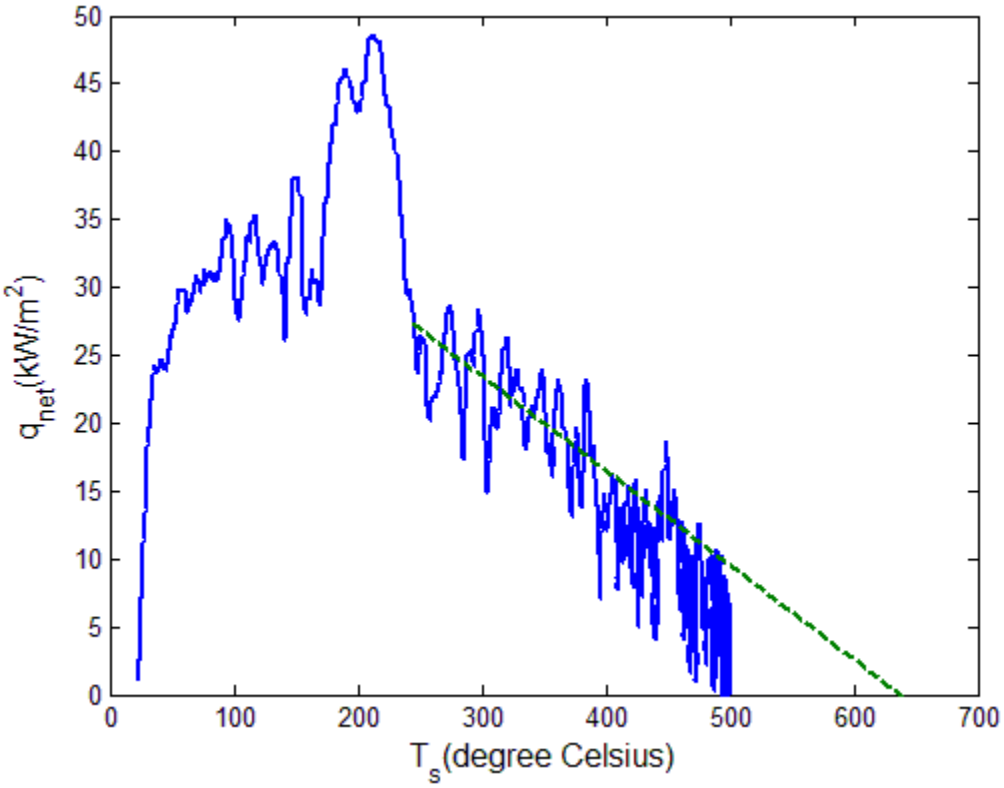

Figure 21. Net heat flux along with linear extrapolation versus surface temperature (50 kW HRR at Lf/2)

2.6.1.2 Comparison to Donaldson et al. [17]

The correlation developed by Donaldson et al. [17] for laminar jets is,

$$Nu_d = \frac{5.4\sqrt{Re_d}}{6.5}\left(\frac{Pr_{fluid}}{Pr_{air}}\right)^{1/3} \quad \text{for } H/d \leq 6.5 \tag{28}$$

$$Nu_d = \frac{5.4\sqrt{Re_d}}{H/d}\left(\frac{Pr_{fluid}}{Pr_{air}}\right)^{1/3} \quad \text{for } H/d > 6.5 \tag{29}$$

In Equation (28), Re_ddenotes the Reynold's no. of the flow, H is the plate to nozzle distance, Pr_{fluid} is the Prandtl no. of impinging fluid, Pr_{air} is the Prandtl no. of air at same temperature. Nusselt number (Nu_d) is calculated using $\boldsymbol{h}$ computed by reference method at stagnation point,

$$Nu_d = \frac{hd}{k} \tag{30}$$

In Equation (30), *k* is the thermal conductivity of the combustion products at the film temperature. Combustion products are assumed to have the same properties as dry air. Thus, $Pr_{fluid} = Pr_{air}$. Re_d is calculated using properties of dry air at film temperature. Values of $\boldsymbol{Nu_d}$ calculated using $\boldsymbol{h}$ are compared with those obtained from Donalson et al.'s correlation in Table 9.

Table 9. $\boldsymbol{Nu_d}$ at stagnation point

	H/d = 3.33	**H/d =5**
Donaldson et al.	51	60
Current study	98	92

The values of $\boldsymbol{Nu_d}$ (Donaldson et al.) are lower than values obtained from current experimental work. This is expected because the values by Donaldson et al. are for laminar jets and they should increase significantly for a turbulent jet. A turbulence coefficient $\boldsymbol{c}$ of 1.72 included in the Donaldson et al.' correlation will give $\boldsymbol{Nu_d}$ values very close to current experimental measurements.

2.6.2 Difference between $\boldsymbol{T_{gas}}$ and AST

In order to determine the domain in which ASTs can be utilized to separate the components of net heat flux, the effect of variation of effective gas radiation temperature on AST for a constant gas temperature is studied. Keeping the gas temperature (T_g) constant at 1100^0C, the effective gas radiation temperature (T_{rad}) is varied over the range $[900^0C, 1200^0C]$, and the net heat flux curves are plotted as per the following equation,

$$q''_{net} = \varepsilon\sigma[T_{rad}^4 - T_s^4] + h(T_g - T_s) \tag{31}$$

The $\boldsymbol{h}$ value used in Equation (31) is equal to 0.094 $kW/(m^2K)$ (stagnation point, H= 0.254 m). AST values are calculated from the plots of net heat flux versus surface temperature and are given in Figure 22. The absorbed irradiation $\left(q''_{abs-irr}\right)$ calculated from T_{rad} is given in Table 10.

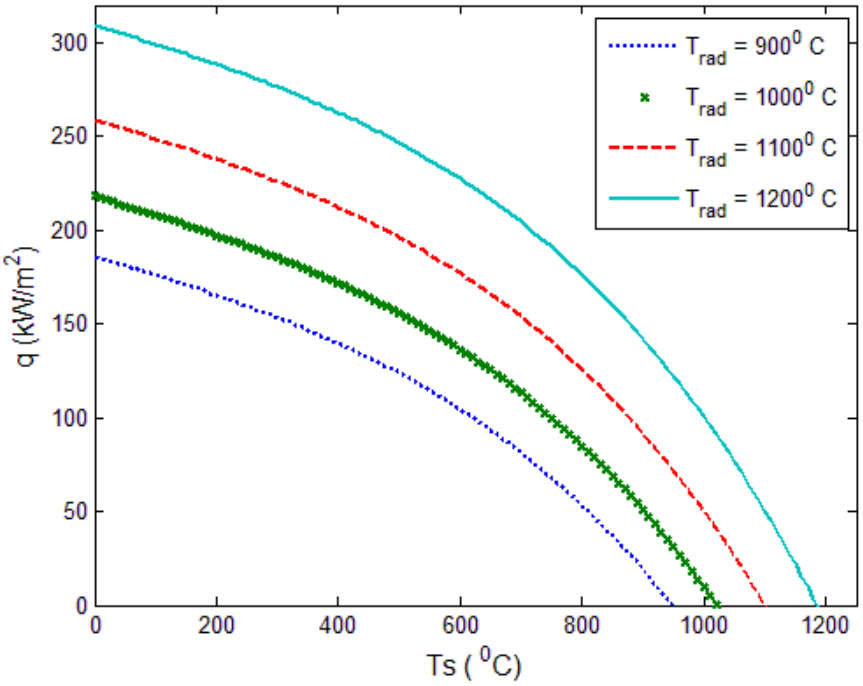

Figure 22. Net heat flux versus surface temperature for various effective radiation gas temperature with $\boldsymbol{T_g = 1100^0\ C}$.

Table 10. AST and absorbed irradiation for various $\boldsymbol{T_{rad}}$

$\boldsymbol{T_{rad}}$ (^{o}C)	AST (^{o}C)	$\boldsymbol{q''_{abs-\,irr}}$ $\left(\boldsymbol{kW/(m^2K)}\right)$
900	950	83
1000	1030	115
1100	1100	155
1200	1190	206

It can be noticed that AST = $\boldsymbol{T_g}$ when $\boldsymbol{T_{rad} = T_g}$. For this case the absorbed irradiation is 155 $\boldsymbol{kW/(m^2K)}$ which is 1.5 times the initial convective heat flux ($\boldsymbol{h \times T_g = 103\ kW/(m^2K)}$) . It can be concluded that AST can be used to estimate the heat flux components in radiation dominated environments (like a furnace) but should not be used in convection dominated environments (like jet impingement heat transfer in ambient environment).

2.7 Conclusions

The HTHFS was found to be an effective heat flux and plate surface temperature measurement tool for the high transient heat fluxes and temperatures experienced in these experiments. The two methods (reference method and slope method) were found to work well for calculating ***h*** in jet flame impingement heat transfer. The methods provided values of ***h*** close to each other and with low relative uncertainty. The drop in ***h*** was less pronounced along the axial direction as compared to the radial direction. AST has been previously shown to be an efficient parameter to represent the combined radiation- convection boundary condition between gas and surface. It serves as a simple and crucial interface between fire and FE structural numerical models. The AST values calculated from measured net heat flux and temperature data gave an estimate of the steady effective radiation and gas temperature. The gas temperature determined from net heat flux and temperature data was a lot higher than the AST. It was observed that the radiation contribution to total heat flux increases as radial distance from the stagnation point increases, although the convection was still the dominant mode of heat transfer for $r/d < 2$. The gas temperature drop along the jet axis seems to be more compared to its drop along the wall jet.

2.8 References

1. Gifford, A., Hubble, D.O., Pullins, C.A., Diller, T.E., Huxtable, S.T., Durable heat flux sensor for extreme temperature and heat flux environments, Journal of Thermophysics and Heat Transfer 24 (2010) 69-76.
2. Vega, T., Lattimer, B.Y., and Diller, T.E., Fire thermal boundary condition measurement using a hybrid heat flux gage, Fire Safety Journal 61 (2013) 127-137.
3. Vega, T., Lattimer, B.Y., and Diller, T.E., Temperature predictions using hybrid heat flux measured boundary conditions, submitted to Fire Safety Journal (2012).
4. Vega, T., Wasson, R., Lattimer, B.Y., and Diller, T.E., Partitioning measurements of Convective and Radiative Heat Flux, International Journal of Heat and Mass Transfer, 84 (2015) 827-838.
5. Wickström U., Robbins A., and Baker G., The use of adiabatic surface temperature to design structures for fire", Journal of Structural Fire Engineering, 2 (2011) 21-28.
6. Hubble, D.O., Diller, T.E., A hybrid method for measuring heat flux, ASME Journal of Heat Transfer 132 (2009) 132-138.

7. Pullins, C., In situ high temperature heat flux sensor calibration, International Journal of Heat and Mass Transfer 53 (2010) 3429-3438.
8. Blevins, L.G., Pitts, W.M., Modeling of bare and aspirated thermocouples in compartment fires, Fire Safety Journal 33 (4) (1999) 239-259.
9. McCaffrey, B.J., Heskestad, G., A robust bidirectional low-velocity probe fore flame and fire application, Combustion and Flame 26 (1976) 125-127.
10. Kidd, C. T. and Nelson, C. G., How the Schmidt-Boelter Gage Really Works, Proc. 41st International Instrumentation Symposium, Research Triangle Park, NC: ISA, 1995, 347-368.
11. Wickstörm U., Duthinh D.,and Mcgrattan K.B., Adiabatic surface temperature for calculating heat transfer to fire exposed structures, Proceedings of 11th Int. Interflam Conference, 3-5 Sept. 2007.
12. Hamins, A. et al., Experiments and Modeling of Structural Steel Elements Exposed to Fire, Federal Building and Fire Safety Investigation of the World Trade Center Disaster, NIST NCSTAR 1-5B, National Institute of Standards and Technology, Gaithersburg, Maryland, US, September 2005.
13. Hindasageri V., Vedula R. P., Prabhu S. V., Heat transfer distribution for impinging methane and air premixed flame Jets, Applied Thermal Engineering 73 (2014) 461-473.
14. M.G. Remie, M.F.G. Cremers, K.R.A.M. Schreel, L.P.H. De Goey, Analysis of the heat transfer of an impinging laminar flame jet, International Journal of Heat and Mass Transfer 50 (2007) 2816-2827.
15. Viskanta R., Convective and radiative flame jet impingement heat transfer, International Journal of Transport Phenomena 1(1998)1–15.
16. Chander Subash, Ray Anjan, Flame impingement heat transfer: A review, Energy Conversion and Management 46 (2005) 2803–2837.
17. Donaldson et al., C.D., Snedeker, R.S., Margolis, D.P., A study of free jet impingement. Part 2. Free jet turbulent structure and impingement heat transfer, Journal of Fluid Mechanics 45 (1971) 477-512.
18. Van der Meer T.H., Stagnation point heat transfer from turbulent low Reynolds number jets and flame jets, Experimental Thermal and Fluid Science 4 (1991)115–26.
19. Baukal C.E., Gebhart B., Oxygen-enhanced/natural gas flame radiation, International Journal of Heat and Mass Transfer 40(11) (1997) 2539–47.

20. Dong L.L., Cheung C.S., Leung C.W., Heat transfer characteristics of premixed butane/air flame jet impinging on an inclined flat surface, Heat and Mass Transfer 39 (2002) 19–26.
21. Milson A., Chigier N.A., Studies of methane air flames impinging on cold plate, Combustion and Flame 21 (1973) 295–305.
22. Kilham J.K., Purvis M.R.I., Heat transfer from hydrocarbon–oxygen flames, Combustion and Flame 16 (1971) 47–54.
23. Fairweather M., Kilham J.K., Mohebi-Ashtiani A., Stagnation point heat transfer from turbulent methane–air flames, Combustion Science and Technology 35 (1984) 225–38.
24. Wu J., Sayed Yagoobi J., Page R.H., Heat transfer and combustion characteristics of an array of radial jet reattachment flames, Combustion and Flame 125 (2001) 955–64.
25. Hoogendoorn C.J., Popiel C.O., Van der Meer T.H., Turbulent heat transfer on a plane surface in impinging round pre-mixed flame jets, Proceedings of 6th international heat transfer conference, Toronto, 4 (1978) 107–12.
26. Baukal C.E., Gebhart B., A review of empirical flame impingement heat transfer correlations, International Journal of Heat and Fluid Flow 17 (1996)386–96.
27. Baukal C.E., Gebhart B., A review of semi-analytical solutions for flame impingement heat transfer, International Journal of Heat and Mass Transfer, 39(1996) 2989–3002.
28. Vlachopoulus, J. and Tomich, J.F., Heat Transfer from a Turbulent Hot Air Jet Impinging on a Flat Plate, Canadian Journal of Chemical Engineering, 49(1971) 462-466.
29. Gardon, R. and Cobonpue, J., Heat Transfer Between a Flat Plate and Jets of Air Impinging on It, International Developments in Heat Transfer, Part II (1963) 454-460.
30. Wasson, R. A. (2014), Partitioning Measurements of Convection and Irradiation Heat Transfer Components from Diffusion Flames Impinging onto Ceilings (Master's thesis), Retrieved from http://hdl.handle.net/10919/50588.

Chapter 3– CONCLUSIONS and RECOMMENDATIONS

3.1 Conclusions

The aim of the experimental work was to study heat transfer coefficient and gas temperature distributions on the surface of flat plates being impinged by a single flame jet. The HTHFS was found to be an effective heat flux and plate surface temperature measurement tool for the high transient heat fluxes and temperatures experienced in these experiments. The two methods (reference method and slope method) were found to work well for calculating ***h*** in jet flame impingement heat transfer. The methods provided values of ***h*** close to each other and with low relative uncertainty. At the axial distances investigated (H/d=3.3 and H/d =5) the heat transfer coefficients were found to have a nearly bell shaped radial distribution. The central cool zone which leads to heat transfer annular maxima in isothermal gas jets was not observed in flame jet for H/d as low as 3.3. Moving from r/d =0 to r/d =2, ***h*** decreased by 37 %. The drop in ***h*** was less pronounced along the axial direction. Upon increasing H/d to 5, the stagnation point ***h*** dropped by only 15%. AST has been previously shown to be an efficient parameter to represent the combined radiation- convection boundary condition between gas and surface. It serves as a simple and crucial interface between fire and FE structural numerical models. The AST values calculated from measured net heat flux and temperature data gave an estimate of the steady effective radiation and gas temperature. The gas temperature determined from net heat flux and temperature data was a lot higher than the AST. It was observed that the radiation contribution to total heat flux increases as radial distance from the stagnation point increases, although the convection was still the dominant mode of heat transfer for r/d < 2. The gas temperature drop along the jet axis seems to be more compared to its drop along the wall jet. Estimated gas temperature dropped by only 15 % from r/d = 0 to r/d = 2. Whereas the drop was measured to be 25 % at stagnation point from H/d =3.3 to H/d =5. The current values of jet heat transfer coefficient compare well with Donaldson et al. [17]'s correlation with a turbulence coefficient of 1.7.

3.2 Recommendations for Future Work

Jet flames impinging on flat surfaces have been studied extensively, but target surfaces of other shapes (cylindrical, hemi-spherical, triangular, etc.) which are of significance to industrial and domestic applications should be studied. Effect of surface treatment on heat transfer has not been

studied in details. Most of the studies have employed circular burners; burners of different geometries need to be used to study levels of initial turbulence generated by burner geometry. The flame temperature in current experiments were measured to be quite high (over 1000^{o} C), which can lead to highly dissociated products, which can reunite upon diffusing to lower temperature regions in the wall jet, and lead to enhanced heat flux in those regions. Measurements were made only at one point in the wall-jet. To notice any TCHR, more points along the wall jet should be included in experimental studies. Studies at higher axial distances and different jet velocities will help study the effects of ***Re*** and ***H/d*** on the radial distribution of heat transfer.

APPENDIX A

Uncertainty calculations in reference method and slope method

An uncertainty analysis was performed on both the reference method and slope method for calculating the heat transfer coefficient. The reference method uncertainty was determined using the law of propagation of uncertainty as outlined in the Guide to the Expression of Uncertainty in Measurement (GUM) [20] whereas the slope method uncertainty was found using a regression uncertainty technique similar to that outlined in Coleman and Steele [A.2]. In the following sections, both the methods of uncertainty calculation in ***h*** are demonstrated for the case: Point 4 (the stagnation point) and H=0.254m (10 inches).

A.1 Relative Uncertainty in Net Heat flux

The uncertainty in net heat flux is required for calculating the uncertainty in heat transfer coefficient by both the methods. The uncertainty in net heat flux is determined using the expression given in Ref. [A.1],

$$u_c^2(q_{net}) = \sum_{i=1}^{N} \left(\frac{\partial q_{net}}{\partial x_i}\right)^2 u^2(x_i) = \sum_{i=1}^{N} c_i^2\, u^2(x_i) \qquad \text{(A.1)}$$

where $x_i's$ are the measured input variables of Equation (8), $c_i's$ are the sensitivity coefficients, and u_{rep} is the uncertainty attributed to repeatability of the experiment.

The sensitivity coefficients are calculated as,

$$c_1 = \frac{\partial q_{net}}{\partial voltage} = \frac{1}{S} \qquad \text{(A.2)}$$

$$c_2 = \frac{\partial q_{net}}{\partial S} = \frac{-voltage}{S^2} \qquad \text{(A.3)}$$

$$c_3 = \frac{\partial q_{net}}{\partial \rho c_p \delta} = \frac{1}{2}\frac{dT}{dt} \qquad \text{(A.4)}$$

$$c_4 = \frac{\partial q_{net}}{\partial \frac{dT}{dt}} = \frac{1}{2}\rho c_p \delta \qquad \text{(A.5)}$$

Table 11 provides the uncertainties in the components of net heat flux.

Table 11. Net heat flux uncertainty components

x_i	Uncertainty type	$u(x_i)$	Comments
voltage	A	7.2 μV	Unbiased sample standard deviation of raw measured voltage
S	B	14.8 $\left(\mu V/(W/cm^2)\right)$	Stated in previous analysis [7]
$\boldsymbol{\rho c_p \delta}$	B	0.03 $\left(Ws/(cm^2K)\right)$	Estimated from previous calibration
$\boldsymbol{\frac{dT}{dt}}$	A	0.086 K/s	Unbiased sample standard deviation of measured data

The relative uncertainty in net heat flux ($u(q_{net})/q_{net}$ (%)) is shown in Figure 23.

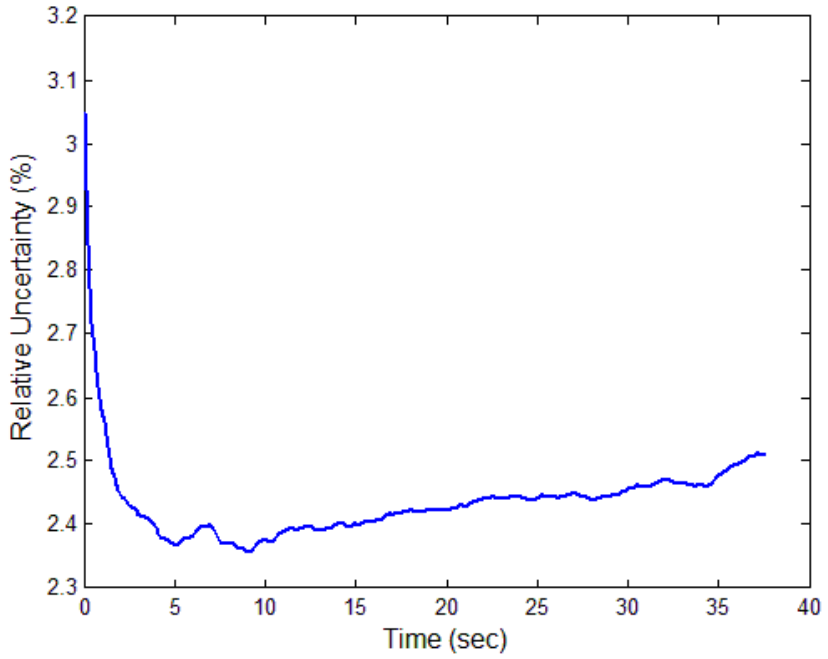

Figure 23. Relative uncertainty in net heat flux at stagnation point

The uncertainty in the measured net heat flux was calculated by applying the law of propagation of uncertainty to the hybrid heat flux method obtained by substituting Equations (6-7) into Equation (8). The relative uncertainty is very high during the first few seconds when the flame is building up. This period is neglected in the computation of heat transfer coefficient and is not shown in Figure 23. The relative uncertainties are low for the rest of the experimental run. It was observed that lower measured heat fluxes resulted in higher relative uncertainties. This trend agrees with those found in literature [A.3].

A.2 Reference Method Uncertainty

A.2.1 Relative Uncertainty in Heat Transfer Coefficient for one reference point

A reference point in time at t=5 sec (i=45th data point), was considered to demonstrate the method of calculation of uncertainty. Note that the tables and figures provided in this section are for this reference point (t=5 sec). Same procedure was followed at all other points in time to calculate their respective uncertainties in ***h***. The reference method uncertainty is expressed as a root sum square of the individual measured uncertainties,

$$u_c^2(h) = \sum_{i=1}^{N}\left(\frac{\partial h}{\partial x_i}\right)^2 u^2(x_i) + 2\sum_{i=1}^{N-1}\sum_{j=i+1}^{N}\frac{\partial h}{\partial x_i}\frac{\partial h}{\partial x_j}u(x_i, x_j) + u_{rep}^2 = \sum_{i=1}^{N} c_i^2 u^2(x_i) + 2\sum_{i=1}^{N-1}\sum_{j+i+1}^{N} c_i c_j u(x_i, x_j) + u_{rep}^2 \quad \text{(A.6)}$$

where ***h*** is the heat transfer coefficient calculated by Equation (11), the x_i , x_j terms are the measured input variables of Equation (11), the c_i , c_j terms are the sensitivity coefficients and u_{rep} is the uncertainty attributed to repeatability of the experiment. The second terms on the right hand side of each equals sign represents any correlated uncertainties in the input variables where $u(x_i, x_j)$ is the covariance of correlated input quantities. The covariance between two input quantities is estimated by,

$$u(x_i, x_j) = \frac{1}{N(N-1)}\sum_{k=1}^{N}(x_{i,k} - \bar{x}_i)(x_{j,k} - \bar{x}_j) \quad \text{(A.7)}$$

where $x_{i,k}$ and $x_{j,k}$ are the individual measurements of the quantities x_i and x_j whereas $\bar{x}_i$ and $\bar{x}_j$ are the mean of the N individual measurements. This correlation must be considered

because a change in T_s will cause a change in q_{net}. The complete expression for the combined standard uncertainty in the value of ***h*** evaluated using the reference method becomes,

$$u_c^2(h) = \left\{c_1^2u^2(q_{net}) + c_2^2u^2\left(q_{net}(i)\right) + c_3^2u^2(\varepsilon_s) + c_4^2u^2(T_s) + c_5^2u^2\left(T_s(i)\right) + 2 \times \left[c_1c_4u(q_{net}, T_s) + c_2c_5u\left(q_{net}(i), T_s(i)\right)\right] + u_{rep}^2\right\} \quad \text{(A.8)}$$

A relative uncertainty is determined by dividing throughout by the heat transfer coefficient. The calculated sensitivity coefficients are defined in Equations (A.9-A.13) and shown in Figure 24. The emissivity sensitivity coefficient has higher values and is not shown in Figure 24.

$$c_1 = \frac{\partial h}{\partial q_{net}} = \frac{-1}{T_s - T_s(i)} \quad \text{(A.9)}$$

$$c_2 = \frac{\partial h}{\partial q_{net}(i)} = \frac{1}{T_s - T_s(i)} \quad \text{(A.10)}$$

$$c_3 = \frac{\partial h}{\partial \varepsilon_s} = \frac{-\sigma(T_s^4 - T_s(i)^4)}{\left(T_s - T_s(i)\right)} \quad \text{(A.11)}$$

$$c_4 = \frac{\partial h}{\partial T_s} = \frac{-(q_{net}(i) - q_{net}) - \varepsilon_s\sigma(3T_s^4 - 4T_s^3T_s(i) + T_s(i)^4)}{\left(T_s - T_s(i)\right)^2} \quad \text{(A.12)}$$

$$c_5 = \frac{\partial h}{\partial T_s(i)} = \frac{(q_{net}(i) - q_{net}) - \varepsilon_s\sigma(T_s^4 - 4T_s(i)^3T_s + 3T_s(i)^4)}{\left(T_s - T_s(i)\right)^2} \quad \text{(A.13)}$$

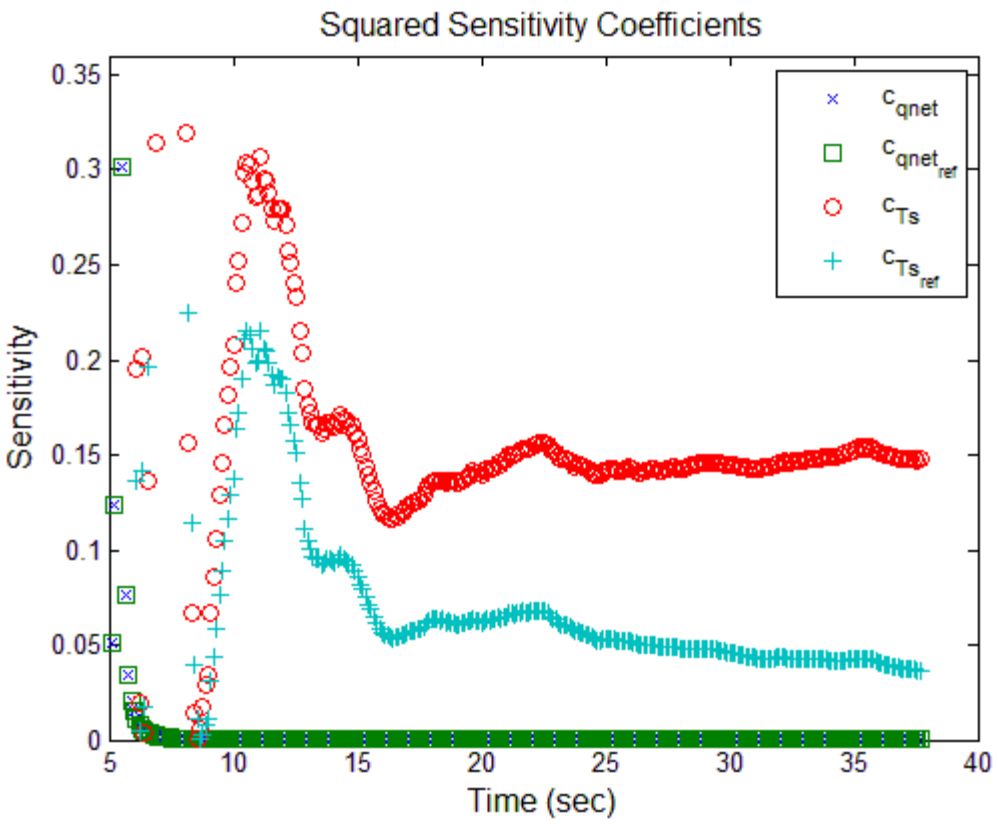

Figure 24 . Reference Method Squared Sensitivity Coefficients.

Table 12 summarizes the individual uncertainty components used to determine the combined uncertainty in the value of ***h*** evaluated using the reference method.

Table 12. Uncertainty Budget for Reference Method Heat Transfer Coefficient

x_i	**Uncertainty type**	$u(x_i)$	**Comments**
q_{net}	A,B –random and bias	2.35– 2.5 % (Figure A.1)	Law of propagation of uncertainty of hybrid heat flux method (Equations 5-7) [A.1]
$q_{net}(i)$	A,B –random and bias	2.37 % (Figure A.1)	Law of propagation of uncertainty of hybrid heat flux method (Equations 5-7) [A.1]
σ	B-bias	0	Assumed no uncertainty
ε_s	B-bias	3%	Unbiased sample standard deviation from three experiments

$\boldsymbol{T_s}$	A-random	0.2- 0.4%	Unbiased sample standard deviation of measured data
$\boldsymbol{T_s}$	B-bias	1.1^0C	Stated by manufacturer
$\boldsymbol{T_s(i)}$	A –random	0.3%	Unbiased sample standard deviation of measured data
$\boldsymbol{u_{rep}}$	B-bias	3%	Repeatability uncertainty calculated from the averages from five experimental runs

As described in Section 2.4.1.1, a certain temperature difference is required for the ***h*** values calculated by reference method to become finite and constant. For the current point, this was observed to be achieved for all data points collected post 18 seconds. Therefore, all the points falling after 18 seconds are taken into consideration for evaluation of ***h***. Figure 25 shows the relative uncertainties in heat transfer coefficient after 18 seconds. The relative uncertainties are infinitely high for data points lying within 5 seconds of the reference point. This points to the fact that a certain temperature difference is required the between points used in ***h*** calculation by Equation (11) to reduce uncertainty below acceptable limits. The relative uncertainty drops to 7 % by the end of experimental run. It is to be noted that higher the temperature difference between points used for ***h*** calculation by Equation (11), lesser the relative uncertainty. The greatest contributors to reference method uncertainty were $q_{net}\ and\ q_{net}(i)$. The sensitivity coefficients of T_s and $T_s(i)$ were similar and more negative than those of $q_{net}\ and\ q_{net}(i)$. The sensitivity coefficients of emissivity rise to very high values (~ -12) by the end of experiment, but the contribution of emissivity uncertainty to combined uncertainty is still very low due to its relatively low value($u(\varepsilon_s) = 0.023$). The sensitivity coefficients for all input quantities fall as time goes on except emissivity which shows opposite trend. This is because all the sensitivity coefficients have the change in gauge surface temperature from its value at time, t=5 sec, in the denominator.

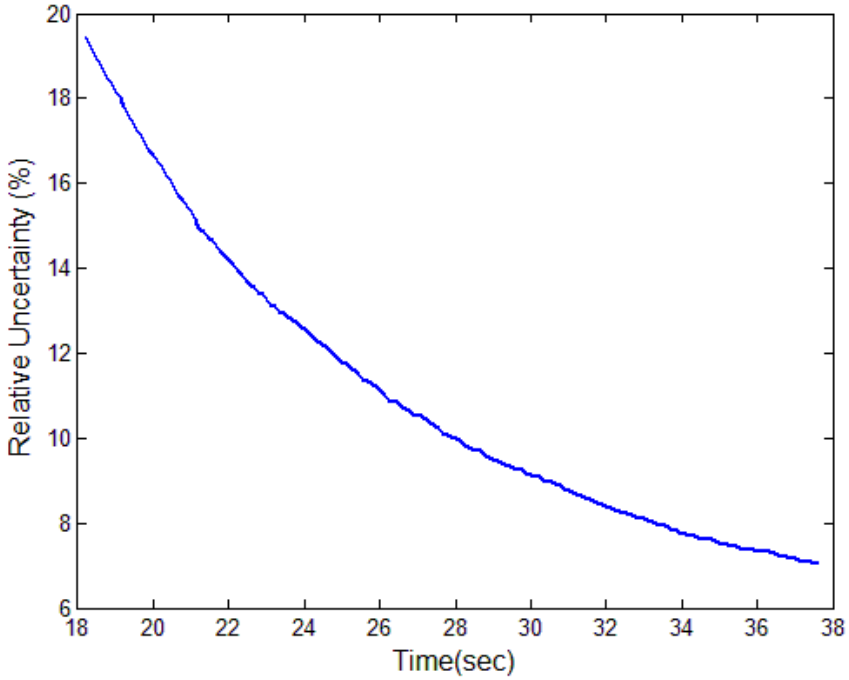

Figure 25. Relative Standard Uncertainty in Reference Method Heat Transfer Coefficient at reference point (t =5 sec)

This value increases with time, thus decreasing the sensitivity coefficients to values smaller than one. The emissivity sensitivity coefficient has the difference between gauge surface temperature raised to power 4 and its initial value raised to power 4 in the numerator which supersedes the decrease due to increase in denominator value. An ***h*** value at this reference point is obtained by taking the mean of the ***h*** values in the interval shown in Figure 25. The value of 95 % level of confidence (k=2) relative uncertainty is 23 % ($\pm 0.022\ kW/(m^2K)$) of the overall heat transfer coefficient value of 0.094 $kW/(m^2K)$.

A.2.2 Relative Uncertainty in Overall Heat Transfer Coefficient

The method described in section A.2.1 was followed at each reference point in time range 5-22 seconds, and a 95% level of confidence (k=2) relative uncertainty in ***h*** at each point was obtained. These are shown in Figure 26. It is observed from Figure 26, that relative uncertainty increases as measured net heat flux decreases. This indicates it is more precise to use the reference method to get ***h*** during the initial stages of the experiment were heat fluxes are high.

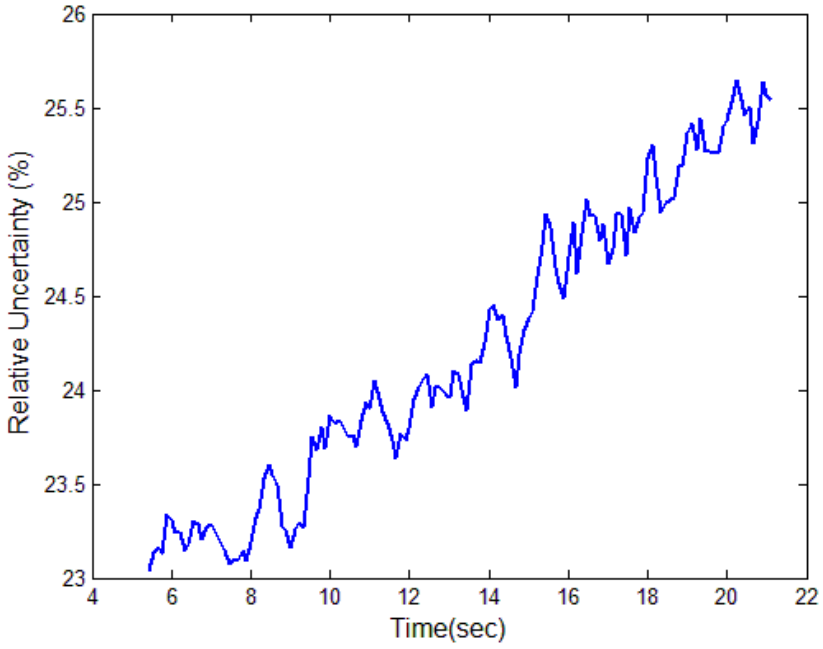

Figure 26. 95% Level of Confidence (k=2) Relative Uncertainty in Reference Method Heat Transfer Coefficient at all Reference Points

As described in Section 2.4.1.1, an overall heat transfer coefficient value was calculated by taking a mean of the average heat transfer coefficient values calculated at all reference points. Equation (A.6) is used to calculate the combined standard uncertainty in this h, which is then multiplied by a coverage factor (k) of 2 (assuming a normal probability distribution) to give the 95 % level of confidence relative uncertainty. **Its value was found to be 24.2 % ($\pm 0.023\ kW/(m^2K)$) of the overall heat transfer coefficient value of 0.094 $kW/(m^2K)$.**

A.3 Slope Method Uncertainty

Quantifying uncertainty in slope method requires quantifying uncertainty in a linear regression. The method used is similar to that outlined by Coleman & Steele [A.2]. This method includes both random and bias uncertainties as well as any correlated bias uncertainties in the regression variables. The 95 % level of confidence uncertainty equation for the slope in a linear regression equation is given as,

$$U_h^2 = 2^2 \left[\left(\frac{\partial h}{\partial Y}\right)^2 u^2(Y)_{bias} + \left(\frac{\partial h}{\partial Y}\right)^2 u^2(Y)_{rando} + \left(\frac{\partial h}{\partial X}\right)^2 u^2(X)_{bias} + \left(\frac{\partial h}{\partial X}\right)^2 u^2(X)_{random} + 2\left(\frac{\partial h}{\partial X}\right)\left(\frac{\partial h}{\partial Y}\right) u(X,Y)_{bias}\right] \quad \text{(A.14)}$$

where, Y is the exposure heat flux to the gauge defined as,

$$q''_{exp} = q''_{net} + \sigma \varepsilon_s T_s^4 \qquad \text{(A.15)}$$

X is the measured gauge surface temperature, ***h*** is the heat transfer coefficient, and the partial derivatives are the sensitivity coefficients of ***h***. The first four terms take into account the random and bias uncertainty in the exposure heat flux as well as the gauge surface temperature. The last term accounts for the correlated bias uncertainties in the exposure heat flux and the gauge surface temperature. These terms must be accounted for since q''_{exp} is calculated using T_s . The uncertainty for the exposure heat flux was determined using the same methodology as for the net heat flux described in section A.1. This uncertainty was determined to be dominated by the net heat flux uncertainty, with little contribution from the gauge surface temperature uncertainty and the correlation term. The random and bias uncertainties in the surface temperature were the same values as specified in Table 12. A perturbation technique was employed to determine the sensitivity coefficients. To determine the sensitivities, numbers were added in 1% increments from 1-10% of each data point for the input variables. Table 13 summarizes the sensitivity coefficients. Exposure heat flux and gauge surface temperature covariance was calculated using Equation (A.7).

Table 13. Sensitivity Coefficients of Slope Method

$\frac{\partial h}{\partial q''_{exp}}\left(\frac{q''_{exp}}{h}\right)$	$\frac{\partial h}{\partial T_s}\left(\frac{T_s}{h}\right)$
1.0	-0.99

The sensitivity coefficients show that the uncertainty in heat transfer coefficient is more sensitive to a change in the gauge surface temperature than the exposure heat flux. The relative uncertainty of slope method is shown in Figure 27.

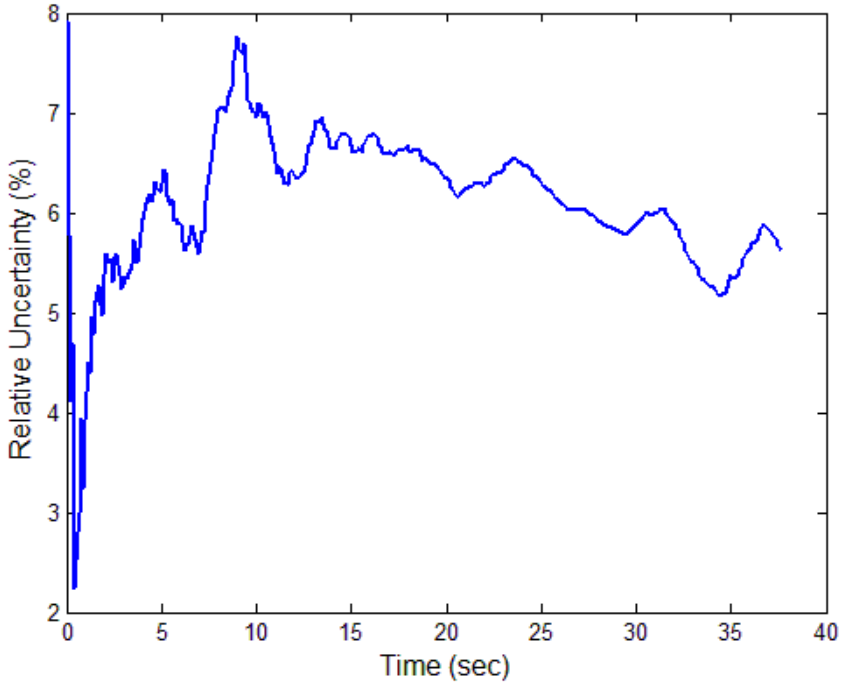

Figure 27. The 95% level of confidence (k=2) Relative Uncertainty in the slope method computed *h*

An average value of 6.42 % was calculated on values calculated after time, t = 10 seconds. **The 95 % level of confidence (k=2) relative uncertainty in slope method calculated *h* is $\pm$ 6.2% ($0.006\ kW/(m^2K)$))of the calculated value of 0.089 $kW/(m^2K)$.** The slope method uncertainty is dominated by exposure heat flux uncertainty with a small contribution from gauge surface temperature uncertainty and a small negative contribution from the correlated term.

[A.1] JCGM 100:2008, Evaluation of measurement data-Guide to the expression of uncertainty in measurement (GUM), first ed., JCGM, 2008.

[A.2] Coleman, H.W. and Steele, W.G., "Experimentation, Validation, and Uncertainty Analysis for Engineers", Third Edition, John Wiley & Sons, Inc., Hoboken, NJ, 2009.

[A.3] Bryant, R. Womeldorf, C., Johnsson, E., Ohlemiller,T.,"Radiative Heat Flux Measurement Uncertainty", *Fire and Materials*, **27**, pp.209-222, 2003.

APPENDIX B

Heat Transfer Coefficient and AST values calculated for test repetitions

The measured ***h*** and computed AST values for the five test repetitions at each point are given in the following tables for the two experimental configurations: H=0.254 m and H = 0.381 m.

B.1 Axial Distance between Burner and Plate surface, H=0.254 m

B.1.1 Heat Transfer Coefficient

Table 14. Stagnation point

Computed heat transfer coefficients at stagnation point (H=0.254m)

Test #	1	2	3	4	5	**Average**
Heat transfer coefficient (kW/m^2K) Reference Method	0.0970	0.0941	0.0936	0.0942	0.0922	**0.0942**
Heat transfer coefficient (kW/m^2K) Slope method	0.0958	0.0845	0.0882	0.0896	0.0879	**0.0892**

Point 3 (2 inches above the stagnation point) & **Point 5** (2 inches below stagnation point):

The corrected gas temperatures for both points were observed to become nearly constant at 730^o C after 7 seconds. The set of data points after time t= 7 sec ($80^0\ C \leq T_s \leq 500^0 C$) were considered for calculating the heat transfer coefficient at these points. It was noticed that a temperature difference of ΔT =200^o C or higher was required for the reference method to provide finite values of '***h***'. The results of the slope methods and the reference method are shown in Table 15.

Table 15. Computed heat transfer coefficients (kW/m^2K) at points 2 inches above (point 3) & 2 inches below (point 5) stagnation point

	Point 3		Point 5	
Test #	Reference Method (kW/m^2K)	Slope method (kW/m^2K)	Reference Method (kW/m^2K)	Slope method (kW/m^2K)
1	0.0784	0.0764	0.0758	0.0798
2	0.0790	0.0814	0.0809	0.0804
3	0.0798	0.0785	0.0786	0.0784
4	0.0765	0.0751	0.0729	0.0785
5	0.0771	0.0752	0.0791	0.0754
Average	0.0782	0.0773	0.0775	0.0785

Point 2 (4 inches above stagnation point) & **Point 6** (4 inches below stagnation point):

The corrected gas temperature at both these points seems to be steady around 550° C after a time-period of 9 seconds; at this point in time, the gauge top surface temperature is around 70° C. Thus, the set of data points having gauge top surface temperature higher than 70° C were used for analysis ($70^0\ C \leq T_s \leq 450^0 C$). From analysis of ***h*** values computed using the reference method, it was noticed that a temperature difference (ΔT) of over 150° C is required to obtain finite and constant 'h' values. Points for the reference method analysis were selected based upon this temperature difference criterion. The results of heat transfer coefficient calculation for this point using all the methods are shown in Table 16.

Table 16. Computed heat transfer coefficients at points 4 inches above (point 2) & 4 inches below (point 6) stagnation point

	Point 2		Point 6	
Test #	Reference Method (kW/m^2K)	Slope method (kW/m^2K)	Reference Method (kW/m^2K)	Slope method (kW/m^2K)
1	0.0641	0.0613	0.0657	0.0655
2	0.0680	0.0663	0.0680	0.0669
3	0.0699	0.0649	0.0627	0.0645
4	0.0672	0.0624	0.0643	0.0606
5	0.0572	0.0569	0.0673	0.0672
Average	0.0653	0.0624	0.0656	0.0649

Point 1 (6 inches above stagnation point) & **Point 7** (6 inches below stagnation point):

It was observed that the corrected gas temperature gets fairly constant after 12 sec at 425° C; the gauge top surface temperature at this time is around 90° C. The set of data points having gauge top surface temperature higher than 90° C were used for analysis ($90^0\ C \leq T_s \leq 350^0 C$). From analysis of ***h*** values computed using the reference method, it was noticed that a temperature difference (ΔT) of over 100° C is required to obtain finite and constant ***h*** values. Points for the reference method analysis were selected based upon this temperature difference criterion. The results of heat transfer coefficient calculation for this point using all the methods are shown in Table 17.

Table 17. Computed heat transfer coefficients at points 6 inches above (point 1) & 6 inches below (point 7) stagnation point

	Point 1		Point 7	
Test #	Reference Method (kW/m^2K)	Slope method (kW/m^2K)	Reference Method (kW/m^2K)	Slope method (kW/m^2K)
1	0.0506	0.0507	0.0568	0.0547
2	0.0504	0.0440	0.0493	0.0520
3	0.0460	0.0442	0.0452	0.0505
4	0.0432	0.0414	0.0523	0.0570
5	0.0513	0.0442	0.0421	0.0423

Average	0.0483	0.0449	0.0491	0.0513

B.1.2 Adiabatic Surface Temperature (AST) & Estimated Gas Temperatures

Table 18. AST values at all points (H=0.254m)

Test #	1	2	3	4	5	Mean (^{o}C)
Point 1	675	665	668	669	687	**673**
Point 2	750	758	765	762	761	**759**
Point 3	801	786	809	802	823	**804**
Point 4	833	853	851	843	843	**845**
Point 5	786	809	822	815	804	**807**
Point 6	756	759	776	747	757	**759**
Point 7	672	673	687.25	676	685	**679**

Table 19. Estimated Gas Temperatures at all points (H=0.254m)

Test #	1	2	3	4	5	Mean (^{o}C)
Point 1	896	963	952	956	941	**942**
Point 2	986	1005	993	1015	983	**996**
Point 3	1022	1027	1033	1014	1043	**1028**
Point 4	1055	1089	1026	1075	1064	**1062**
Point 5	1047	1038	1050	1035	1020	**1038**
Point 6	980	991	970	985	997	**985**
Point 7	923	932	914	940	911	**924**

B.2 Axial Distance between Burner and Plate surface, H=0.381 m

B.2.1 Heat Transfer Coefficient

The corrected gas temperature was found to get steady around 800^o C after 10 seconds. A value of $\Delta T = 150^0\ C$ is required for reference method to report steady values. The $\boldsymbol{h}$ values are given in Table 20.

Table 20. Heat Transfer Coefficient at stagnation point (H=0.381 m)

Test #	1	2	3	4	5	Mean
Reference Method (kW/m^2K)	0.0786	0.0808	0.0791	0.0763	0.0851	**0.08**
Slope method (kW/m^2K)	0.0765	0.082	0.0837	0.0801	0.0822	**0.081**

B.2.2 AST and Estimated Gas Temperatures

Table 21. AST and Estimated Gas Temperatures at stagnation point (H=0.381 m)

Test #	1	2	3	4	5	Mean
T_{AST} (deg. C)	620	625	624	639	650	**632**
T_{gas} (deg. C)	842	855	825	829	847	**840**

APPENDIX C

Calibration procedures, Gauge Sensitivities and Emissivity

C.1 Radiation Calibration using Lamp

C.1.1 Introduction

This document serves as a guideline for all heat flux gauge lamp calibrations in 100V. It is best to try and follow these procedures to ensure consistent calibration methods are being used.

C.1.2 Equipment

Halogen Lamp:

- USHIO J120V-250W/79 halogen bulbs
- Life of 2000 hours
- Lamp has focal point of 1.25" away from its face

Model SC-10T Variac:

- 0-130 VAC
- Max 1000W
- 117VAC, 60 Hz input

HP 3468A True RMS Multimeter:

- We want to measure AC

HTHFS and SB gauge with holders:

- Each has their own plate holder. We want to figure this out.
- SB gauge has sensitivity of 625.19 uV/(W/cm^2). It is used to calibrate the lamp.

Gage Holster:

- Same gage holster used for both SB and HTHFS

NI cDAQ 9172:

- 24 bit Sigma delta A/D
- 9213 thermocouple module
- 9219 voltage module
- HTHFS TC1 and TC2 leads, water temp lead

Dell laptop

- Has the necessary LabVIEW files on it

Ice in a bucket

C.1.3 Experimental Setup

1. Gather all needed equipment.

2. Configure the lamp and the gage holster facing towards each other.

3. Connect water hoses to lamp.

    a. This requires that two hoses are connected to the water pumps and then to one side of the lamp (provide cooling water). Another two hoses are connected to the other side of the lamp and are allowed to empty into the water bin (take cooling water away).

4. Connect water hoses to gauge.

    a. For the SB gauge, there are 4 hoses total. Two hoses should be hooked up to one pump to provide cooling water to both the gage and the plate. The other two hoses are free to the bin to take the cooling water away from both the gauge and the plate.

    b. For the HTHFS, there are 5 hoses. One hose provides cooling water to the gage and is thus connected to a pump while all other hoses are free to the water bin.

5. Mount gauge into plate holder. Use thermal grease to reduce contact resistance. Screw gauge into holder.

6. Mount gauge and holder into gauge holster. Use machinist ruler to ensure gage face is 1.25" away from lamp face. Tighten bolts on holster so that it becomes fixed to lamp base (does not move/wiggle).

7. Plug in lamp and multimeter to variac (brown to red and blue to black). Make sure multimeter and variac are also plugged in.

8. Connect all lead wires to daq (See Figure 1).

    a. SB gage lead wires are white (+) and black (-). These leads go connected to the 9219 module. Connect the leads to any desired channel but ensure that the white wire (+) is connected to terminal 4 (high signal) and the black wire (-) is connected to terminal 5 (low signal).

    b. For the HTHFS, the yellow wire (Chromel) is the positive lead and the red wire (Alumel) is the negative lead. When connecting connectors together, positive side goes to positive and negative goes to negative. These go connected to the 9213 module for temperature readings and then connected to the 9219 for heat flux readings. See figure below for setup.

    c. Make sure to connect a TC for the water temp.

9. Configure Labview file to read channels as they are hooked up and for a sampling rate of 1Hz.

10. To do this, open the labview file titled “HTHFS Radiation Calibration” or “SB Radiation Calibration” depending on which you are performing. Open the DAQ Assistant block and ensure that the physical channels correspond to the actual channel.

11. You are now ready to calibrate.

C.1.4 Calibration Procedure

1. Turn on daq and allow warm up of 15 min.

2. Check to make sure all hoses are connected properly.

3. Check that all lead wires are connected properly.

4. Check to make sure VI channels correspond to actual channels.

5. When the system is at thermal equilibrium with the surroundings (Before water pumps or heater are turned on) run the VI to make sure text file of raw data is being written.

6. Collect data at thermal equilibrium for at least 2 min prior to ramping up the voltage. This is the voltage offset in the system and will be subtracted off of the data (Subtracting bias).

7. Ramp up the voltage on the variac to desired setting and allow for entire system to reach steady state (no change in temperature >0.2 C for 5 min). Repeat for desired voltage levels.

    a. Note: The voltage level is entirely up to the calibrator, however 5 measurements in the range of 40-120V should be fine. We expect the response to be approximately linear to the input voltage.

8. Record all voltage levels. These will be used later in the code.

9. Be sure to monitor the water temperature. If it rises above room temp (22-26 C), add ice to the water bin. It is important to keep the gauge close to room temperature to ensure that convection is kept to a minimum level.

C.1.5 Post Processing

This can be done in Excel or Matlab.

<u>For SB</u>

If you are using the SB gauge to calibrate the lamp, you will

1. Average the baseline measurements (first 2 min) and subtract this average from all of the voltage output data. This gets rid of offset voltage.

2. Go through data and identify the end time of the steady state events.

3. Average the steady state data (example: the end of the steady state event was at 500 seconds so I am going to average the last 60 measurements from 440 to 500).

4. Multiply this by 10^6 to put data into micro-Volts (uV).

5. Take this and divide by the sensitivity (625.19 uV/(W/cm^2)) to get *absorbed* heat flux (heat flux absorbed by sensor).

6. We can now calculate the *incident* heat flux to the sensor by dividing by the emissivity which is 0.94 for the black paint in the lab. (Recall our assumption of negligible convection.)

7. Plot the input voltage versus the incident heat flux. Use a 4^{th} degree polynomial fit to find the coefficients we will use to relate input voltage to incident heat flux for future calibrations.

<u>For HTHFS</u>

If you are calibrating a HTHFS, you will

1. Average the baseline measurements (first 2 min) and subtract this average from all of the voltage output data. This gets rid of bias voltage.

2. Go through data and identify the end time of the steady state events.

3. Average the steady state data (example: the end of the steady state event was at 500 seconds so I am going to average the last 60 measurements from 440 to 500).

4. Multiply this by 10^6 to put data into micro-Volts (uV).

5. Use the coefficients from the SB calibration and evaluate the polynomial equation at the voltage levels used during the calibration. This gives the *incident* heat flux of the lamp.

6. We can now calculate the *absorbed* heat flux to the sensor by multiplying by the emissivity which is 0.94 for the black paint in the lab. (Recall our assumption of negligible convection.)

7. Divide the mean SS voltage output from the gage by the absorbed heat flux to get sensitivities in uV/(W/cm^2).

C.2 Thermal Storage Calibration using Lamp

C.2.1 Introduction

This document serves as a guideline for all HTHFS thermal storage lamp calibrations. It is best to try and follow these procedures to ensure consistent calibration methods are being used.

C.2.2 Equipment

Halogen Lamp:

- USHIO J120V-250W/79 halogen bulbs
- Life of 2000 hours
- Lamp has focal point of 1.25" away from its face

Model SC-10T Variac:

- 0-130 VAC
- Max 1000W
- 117VAC, 60 Hz input

HP 3468A True RMS Multimeter:

- We want to measure AC

HTHFS with alumina surrounding:

- The gauge is mounted in a piece of alumina to provide for insulation.

Gauge Holster:

- Same as for differential calibration

NI cDAQ 9172:

- 24 bit Sigma delta A/D
- 9213 thermocouple module
- 9219 voltage module
- HTHFS TC1 and TC2 leads, reflector temp lead

Pneumatic Cylinder:

- Clippard SDD-17-9
- Max 250 psi
- 1 1/16" bore
- 9" stroke

2 Solenoid Valves

- MAC 224B-531BAA
- 0.5 C_v
- Vacuum to 150psi

- 3 port, 2 directions—(Port 1 inlet, port 2 outlet, port 3 exhaust)
- 24 VDC (either on or off)

2 DC Power supplies (For valves)

- 24 VDC

Dell laptop

- Has the necessary LabVIEW files on it---Slug_calibration VI

C.2.3 Experimental Setup

12. Gather all needed equipment.

13. Configure the lamp and the gauge holster facing towards each other.

14. Connect water hoses to lamp.

    a. This requires that two hoses are connected to the water pumps and then to one side of the lamp (inlets to provide cooling water). Another two hoses are connected to the other side of the lamp and are allowed to empty into the water bin (outlets to remove cooling water).

15. Mount gauge into insulation slot. Use #1 bolts ~1 ¼" long with small metal plate on back.

16. Mount gauge and insulation into gauge holster. Use machinist ruler to ensure gauge face is 1.25" away from lamp face. Tighten bolts on holster so that it becomes fixed to lamp base (does not move/wiggle).

17. Mount pneumatic cylinder (with brackets) onto base plate with screws 10-32-1/2". Also mount solenoid valves onto base plate with 10-32-2" screws. Clamp base plate to table; ensure sheet metal is covering the lamp and gauge.

18. Connect all lead wires to daq .

    a. For the HTHFS, the yellow wire (Chromel) is the positive lead and the red wire (Alumel) is the negative lead. When connecting connectors together, positive side goes to positive and negative goes to negative. These go connected to the 9213 module for temperature readings and then connected to the 9219 for heat flux readings. See figure below for setup.

    b. Make sure to connect a TC for the water temp.

19. Hook hose up to airline. Plug valve leads into DC supplies.

20. Plug in lamp and multimeter to variac (brown to red and blue to black). Make sure multimeter and variac are also plugged in.

21. Configure Labview file to read channels as they are hooked up and for a sampling rate of 2 Hz.

    a. To do this, open the labview file titled "HTHFS Slug Calibration". Open the DAQ Assistant block and ensure that the physical channels correspond to the actual channel.

22. You are now ready to calibrate.

C.2.4 Calibration Procedure

10. Turn on daq and allow it to warm up for 15 min.

11. Check to make sure all hoses are connected properly.

12. Check that all lead wires are connected properly.

13. Check to make sure VI channels correspond to physical channels.

14. When the system is at thermal equilibrium with the surroundings (Before water pumps or heater are turned on) run the VI to make sure a text file of raw data is being written.

15. Collect SS data at thermal equilibrium for at least 2 min prior to ramping up the voltage. This is the voltage offset of the system and will be subtracted off of the raw data.

16. Actuate the rear solenoid by supplying power to it so that piston rod is fully extended, thus covering the gauge from the lamp. Remove power from the valve.

17. Ramp up the voltage on the variac to desired setting and allow it to reach SS (1-2 seconds). When ready, apply power to the front valve to actuate the piston backwards, uncovering the gauge. Allow gauge to be exposed for 30 seconds before covering up again and shutting variac off. Allow gauge to reach equilibrium before next test. Repeat for desired voltage levels.

    a. Note: The voltage level is entirely up to the calibrator, however 5 measurements in the range of 40-120V should be fine. I used [40V, 60V, 80V, 100V, 120V].

18. Record all voltage levels. These will be used later in the code.

C.2.5 Post Processing

8. Average the baseline measurements (~first 2 min) and subtract this average from all of the voltage output data. This gets rid of offset voltage.

9. Multiply this by 10^6 to put data into micro-Volts (uV).

10. Enter all voltage levels used during testing as well as sensor differential sensitivities and sample rate used in Hz.

11. Use the lamp coefficients from the SB calibration and evaluate the polynomial equation at the voltage levels used during the calibration. This gives the *incident* heat flux.

12. We can now calculate the *absorbed* heat flux to the sensor surface by multiplying by the emissivity which is 0.94 for the black paint in the lab. (Recall our assumption of negligible convection.)

13. Go through data and identify the start and end time (or duration) of each event.

14. Pick out heat flux data and temperature data which only correspond to the individual thermal events.

15. Subtract the initial temperature for each event from both TC measurements.

16. Average the two sensor thermocouple measurements to get Tavg.

17. Divide the average temperature by the net heat flux and plot for all voltage levels to get the inverse of the gauge thermal storage.

    a. Use methodology found in slug cal write-up.

18. Fit the plotted line using a linear fit. The inverse of the slope of this line is the thermal storage of the gauge.

C.3 Slug Calibration Calculations

Method 1:

- No heat lost to insulation (perfectly insulated)
- All heat absorbed at surface is stored in the gauge

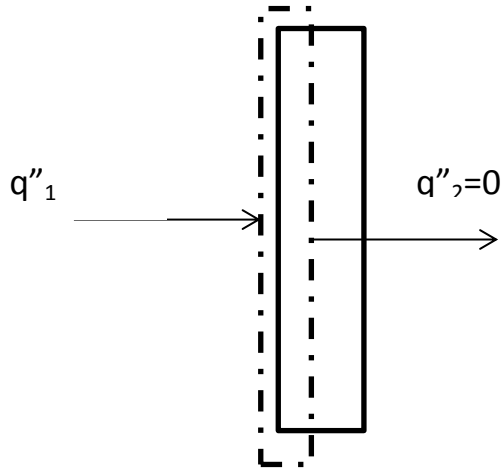

$$\rho c_p V(T - T_i) = q_1^{"} A * t$$

$$\rho c_p \delta(T - T_i) = q_1^{"} * t$$

$$\frac{d}{dt}\left(\frac{T - T_i}{q_1^{"}}\right) = \frac{1}{\rho c_p \delta}$$

T-Average temperature of gauge

T_i-Initial temperature of gauge

$q"_1$-Heat flux from lamp

$\rho c_p \delta$- thermal storage of gauge

Method 2:

– Accounts for energy losses due to re-radiation from gauge surface and heat lost to insulation

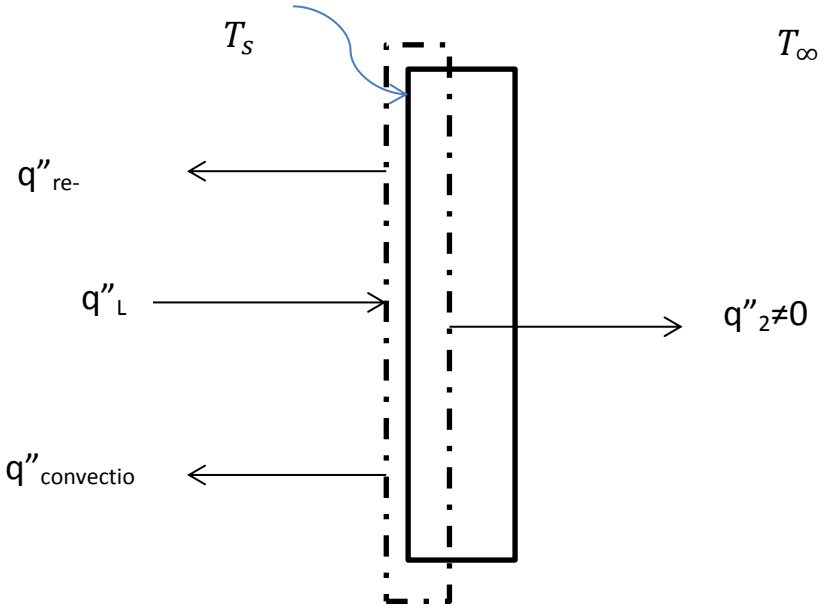

q”$_L$=heat absorbed by surface from lamp

q”$_{re\text{-}radiation}$=re-radiation heat flux from gauge=$\varepsilon_s \sigma T_s^{\,4}$

q”$_{convection}$=convection heat transfer=$h(T_s - T_\infty)$

q”$_2$=heat lost to insulation (calculated using HHF method)

In HHF method:

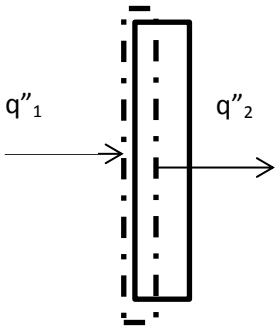

$$q''_{diff} = \frac{q''_1 + q''_2}{2} = output\ from\ HTHFS$$

$$q''_{slug} = \rho c_p \delta \frac{dT}{dt} = q''_1 - q''_2$$

Rearranging and adding to solve for q”$_2$:

$$q_1^{"} + q_2^{"} = 2q_{diff}^{"}$$

$$-q_1^{"} + q_2^{"} = -\rho c_p \delta \frac{dT}{dt}$$

$$q_2^{"} = q_{diff}^{"} - \frac{1}{2}\rho c_p \delta \frac{dT}{dt}$$

Plugging all components into an energy balance on the surface:

$$\rho c_p \delta \frac{dT}{dt} = \mathrm{q}_L^{"} - \mathrm{q}_{re-radiation}^{"} - \mathrm{q}_{convection}^{"} - q_{diff}^{"} + \frac{1}{2}\rho c_p \delta \frac{dT}{dt}$$

$$\frac{1}{2}\rho c_p \delta \frac{dT}{dt} = \mathrm{q}_L^{"} - \mathrm{q}_{re-radiation}^{"} - \mathrm{q}_{convection}^{"} - q_{diff}^{"}$$

Rearranging

$$\frac{d}{dt}\left(\frac{T - T_i}{2\left(\mathrm{q}_L^{"} - \mathrm{q}_{re-radiation}^{"} - \mathrm{q}_{convection}^{"} - q_{diff}^{"}\right)}\right) = \frac{1}{\rho c_p \delta}$$

$$\frac{d}{dt}\left(\frac{T - T_i}{2\left(\mathrm{q}_{net}^{"}\right)}\right) = \frac{1}{\rho c_p \delta}$$

For this calibration, in order to include convection, an estimate of h as well as an estimate of the ambient air is required.

C.4 Non-cooled Hybrid Gauge Calibrations

Voltage input =

40.0017 60.4660 80.3687 100.1147 (V)

Alumel Sensitivities =

485.7698 470.3089 475.5911 482.7669 $\mu V / \left(\frac{W}{cm^2}\right)$

Chromel Sensitivities =

348.2393 337.5046 341.8392 347.1434 $\mu V / \left(\frac{W}{cm^2}\right)$

Average Alumel Sensitvity =478.6092 $\mu V / \left(\frac{W}{cm^2}\right)$

Average Chromel Sensitvity =343.6816 $\mu V / \left(\frac{W}{cm^2}\right)$

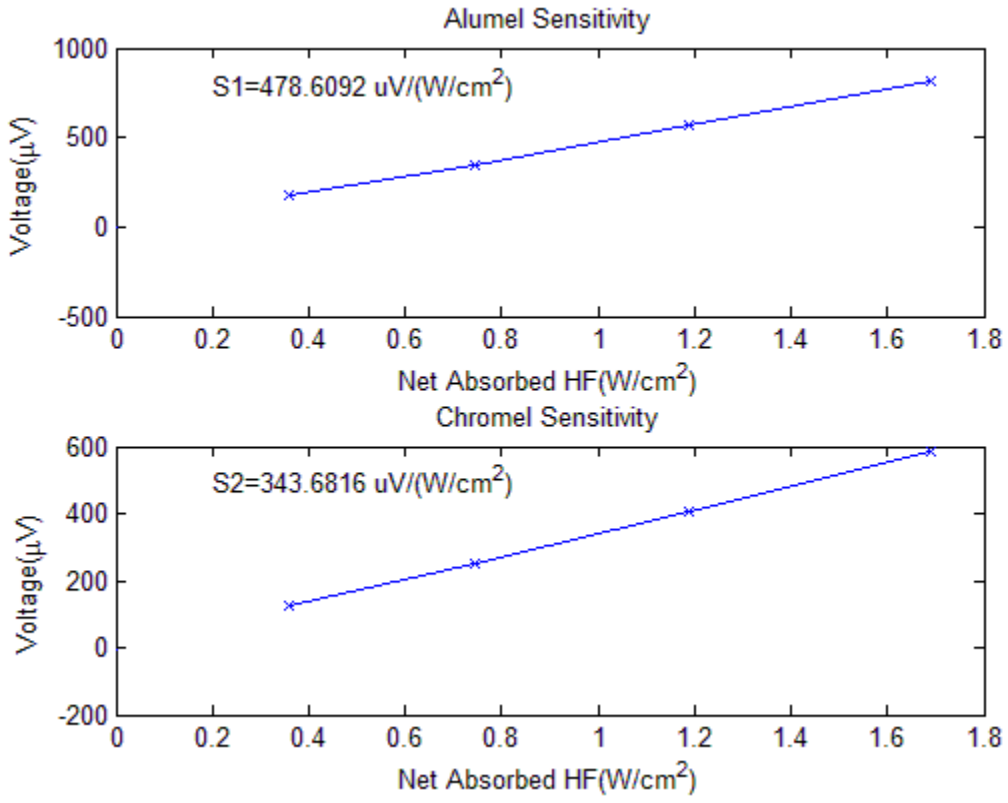

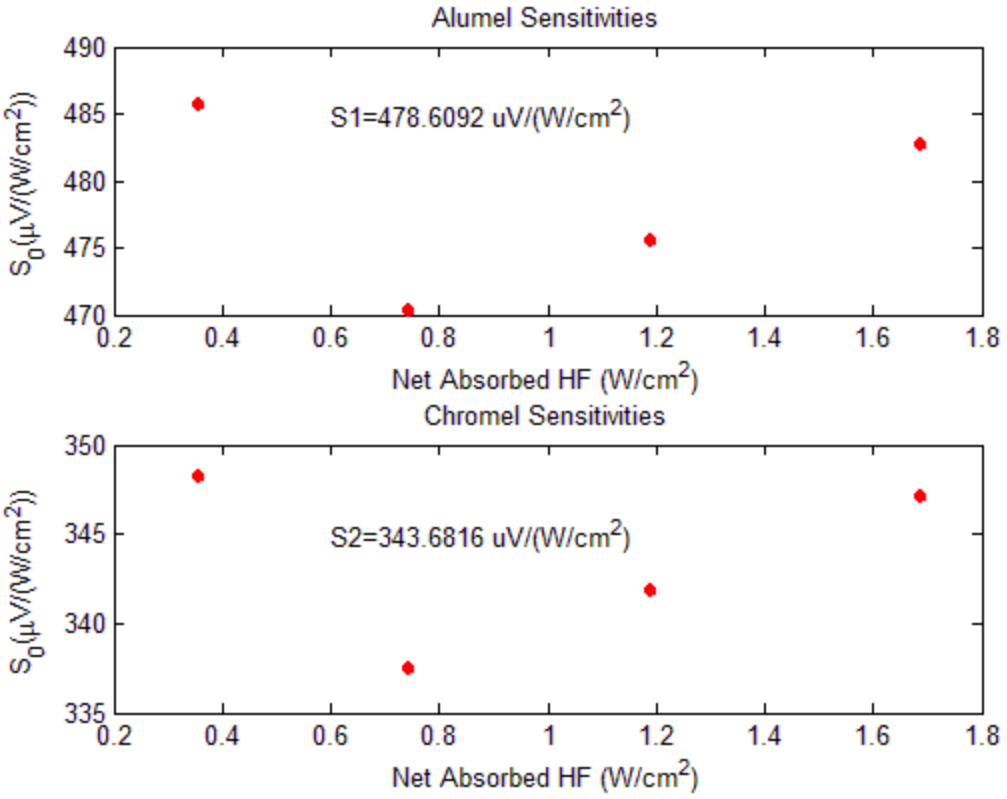
Alumel Sensitivities
S1=478.6092 uV/(W/cm2)
S0(μV/(W/cm2))
Net Absorbed HF (W/cm2)
Chromel Sensitivities
S2=343.6816 uV/(W/cm2)
S0(μV/(W/cm2))
Net Absorbed HF (W/cm2)

C.5 Schmidt Boelter Gauge Calibrations

Voltage input=

40.0803 60.7590 80.0477 96.3103 (V)

Sensitivities =

1.0e+03 *

1.9925 1.9766 1.9575 1.9641 $(\mu V/\left(\frac{W}{cm^2}\right))$

Average Sensitivity =

1.9727e+03 $\mu V/\left(\frac{W}{cm^2}\right)$

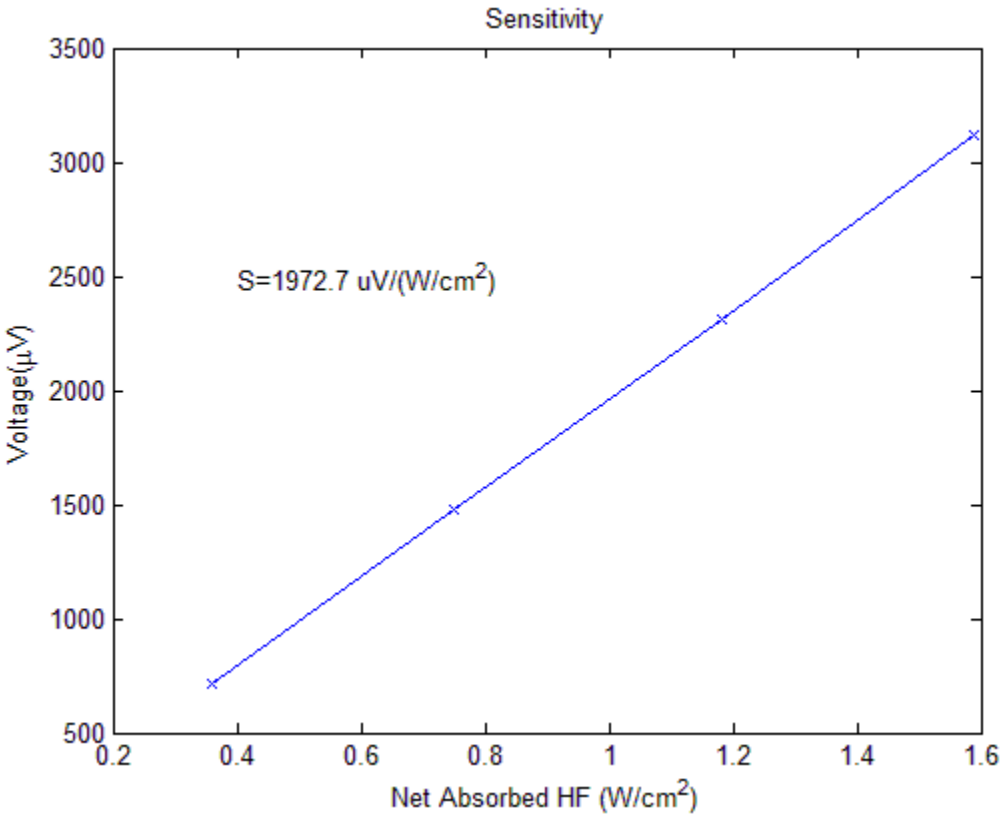

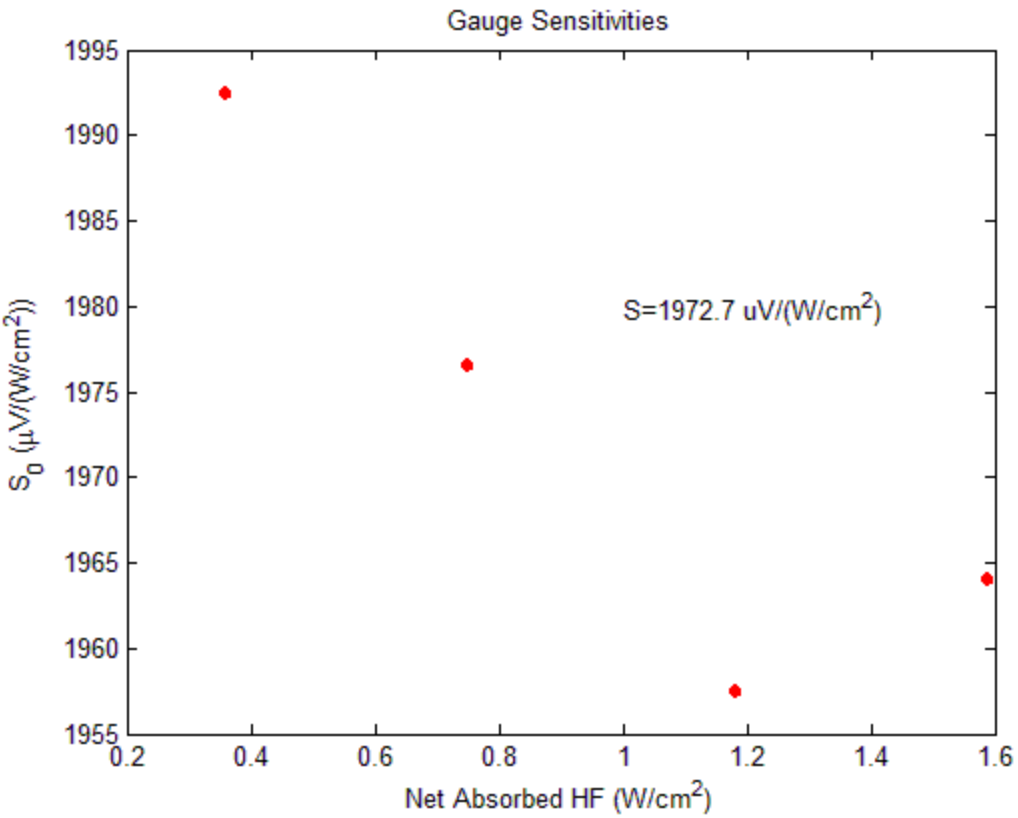
Gauge Sensitivities
1995
1990
1985
1980
1975
1970
1965
1960
1955
0.2
0.4
0.6
0.8
1
1.2
1.4
1.6
S=1972.7 uV/(W/cm2)
S0 (μV/(W/cm2))
Net Absorbed HF (W/cm2)

C.6 Gauge Emissivity Calculations

The gauge was calibrated in the radiative environment two times, once with black paint of known emissivity (0.94) and the next time without paint on.

The results for calibration with black paint have been presented earlier. Given below are the results for calibration without paint on.

Voltage input = 40.4533 60.4643 80.1553 100.1553 (V)

Incident Heat Flux = 0.3890 0.7902 1.2591 1.7976 (kW/m^2)

Heat Flux absorbed = 0.3024 0.5951 0.9673 1.4120 (kW/m^2)

Emissivity = Incident Heat Flux/Absorbed Heat Flux = 0.7775 0.7531 0.7682 0.7855

Taking an average of emissivity values obtained at different voltages,

Emissivity = 0.7711